21GRD02 BIOSPHERE

D5: Good Practice Guide for the simulation and estimation of particle fluxes during minimum solar activity, maximum solar activity and the recent Solar Energetic Particle Events

Organisation name of the lead participant for the deliverable: **BIRA-IASB**

Due date of the deliverable: **M36 (September 2025)**

Actual submission date of the deliverable: 30 September 2025

Confidentiality Status: PU - Public, fully open

Deliverable Cover Sheet

Funded by the European Union. Views and opinions expressed are however those of the author(s) only and do not necessarily reflect those of the European Union or EURAMET. Neither the European Union nor the granting authority can be held responsible for them.

The project has received funding from the European Partnership on Metrology, co-financed from the European Union's Horizon Europe Research and Innovation Programme and by the Participating States.

Good Practice Guide for the simulation and estimation of particle fluxes during minimum solar activity, maximum solar activity and the recent Solar Energetic Particle Events

A. Winant, V. Pierrard

Glossary

ARMs: Atmospheric Response Matrices

AtRIS: Atmospheric Radiation Interaction Simulator

BIRA-IASB: Royal Belgian Institute for Space Aeronomy

CERN: Central European Research Network

CRAND: Cosmic Ray Albedo Neutron Decay

Dst: Disturbance storm time

EPT: Energetic Particle Telescope

GCRs: Galactic Cosmic Rays

GEANT4: GEometry ANd Tracking

GOES: Geostationary Operational Environmental Satellite

IMF: Interplanetary Magnetic Field

LEO: Low Earth Orbit

PI: Principal Investigator

PSF: Planet Specification File

RBs: Radiation Belts

ULF: Ultra Low Frequency

SC: Sudden Commencement

SEP: Solar Energetic Particle

SPAND: Solar Proton Albedo Neutron Decay

SSA: South Atlantic Anomaly

TOA: Top Of the Atmosphere

PDGC: Particle Data Group Code

Contents

21GRD02 BIOSPHERE 1
1 General introduction 4
2 Description of the radiative space environment of the Earth 4
2.1 Radiative space environment of the Earth 4
2.1.1 Galactic Cosmic Rays (GCRs) 4
2.1.2 Solar wind 4
2.1.3 Solar Activity Cycle 5
2.1.4 Magnetic environment of the Earth 5
2.1.5 The Van Allen radiation belts 5
2.1.6 South Atlantic anomaly 6
2.2 Motion of particles in the radiation belts 6
2.2.1 Gyration motion 7
2.2.2 Drift motion 7
2.2.3 Bounce Motion 8
2.3 Adiabatic Invariants 10
2.3.1 The first adiabatic invariant 10
2.3.2 The second adiabatic invariant 11
2.3.3 The third adiabatic invariant 11
2.4 Geomagnetic Coordinates (B, L) 12
2.5 Physical processes in the radiation belts 12
2.5.1 Inner Belt 12
2.5.2 Anisotropic proton fluxes 13
2.5.3 Outer belt 13
2.6 Geomagnetic storms 14
3 Satellite flux data analysis 15
3.1 Open source data 15
3.2 Differential flux and integral flux 15
3.3 Displaying data 16
3.4 Data contamination and data quality 17
3.5 Averaging the data in time 18
3.6 The effects of the event of May 2024. 19
3.7 Prediction of terrestrial radiation belts using deep learning 21
4 Geant4 AtRIS simulations of energetic particle interactions with the atmosphere 21
4.1 What is the Atmospheric Radiation Interaction Simulator (AtRIS) ? 21
4.2 Setting up a simulation 21
4.2.1 Creating the planet 21
4.2.2 Providing the radiation phantoms 22
4.2.3 Providing the primary particle energy binning 22
4.3 How to use AtRIS results ? 22
4.3.1 Ionization and dose rates 22
4.3.2 Secondary particles 24
5 Conclusions 27
6 References 27

1 General introduction

This Good Practice Guide intends to summarize the best way to estimate the space particle fluxes and their interactions with the atmosphere. It provides guidance for the analysis of space radiation fluxes using satellite measurements and for the simulations of their interactions with the terrestrial atmosphere using the AtRIS code. It also provides the most recent results obtained at BIRA-IASB for different solar eruption events and geomagnetic storms, especially during solar cycle 25 which has its maximum in 2025. This guide written in the framework of the EURAMET Biosphere project is made available on the project's website www.euramet-biosphere.eu and promoted in the project's workshops/training events so that users in space physics, radiation and atmospheric communities can easily access these documents for reference and to implement the methods for estimations of spatial energetic fluxes of particles and for atmospheric investigations developed in the project.

2 Description of the radiative space environment of the Earth

This first section aims to provide to the readers a basic understanding of the complex space environment of the Earth, from the Interplanetary Magnetic Field (IMF) to the motion of trapped particles in the Earth's quasi-dipolar magnetic field and the physical processes occurring in the Radiation Belts (RBs) during geomagnetic storms. It is important to note that this guide is not a detailed text book on space physics, as it can be found in *[Pierrard, 2024]* for instance, nor on data processing. Its only purpose is to provide the readers with the necessary tools to understand and facilitate their use of satellite data in the context of the RBs study.

2.1 Radiative space environment of the Earth

2.1.1 Galactic Cosmic Rays (GCRs)

Galactic Cosmic Rays (GCRs) are high-energy particles, mainly protons and helium nuclei that are produced from outside of our solar system. Cosmic radiation is the continuous flow of very high-energy (relativistic) particles, consisting of more than 85% hydrogen nuclei (protons), about 10% alpha particles (helium), some heavier ions and energetic electrons. The neutral part is composed of gamma rays and neutrinos. The energy of charged particles of GCRs that has an influence on atmosphere ionization varies from a few hundred MeV (1 Mega electron Volt= 10^6 eV) to TeV (1 Tera electron Volt = 10^{12} eV). The energy spectrum of cosmic rays has been measured up to 10^{21} eV *[Gaisser et al., 2016]*. Solar cosmic rays are emitted by the Sun during eruptions (energetic particle events), but the most energetic ones, called galactic cosmic rays, come from interstellar space, from the nucleus of our galaxy, from supernovae (explosion of stars) and other extragalactic objects *[Pierrard, 2024]*. When high-energy charged cosmic-ray particles reach the atmosphere, they cause ionization at lower altitudes through complex nucleon-muon-electromagnetic cascades. Atmospheric neutrons generated by cosmic rays (>GeV) are detected by neutron monitors at the surface of the Earth. These galactic cosmic rays form a continuous source of radiation that constantly ionizes the Earth's atmosphere with a maximum rate appearing around 15 km. Due to the geomagnetic field shielding that produces a cut-off, the ionization appears mainly at high latitudes.

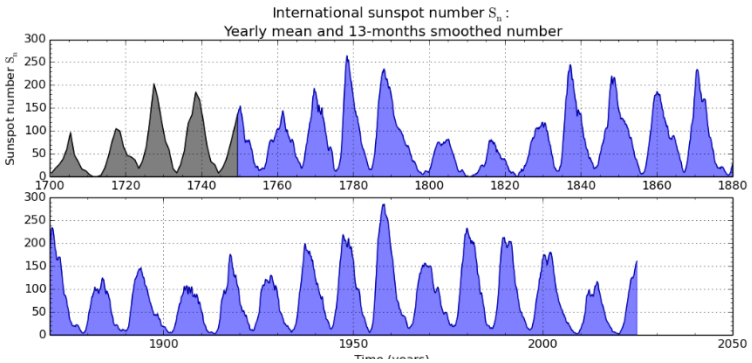

Figure 1:Number of sunspot following the solar cycle of 11 years. Image from sidc.be

2.1.2 Solar wind

In the solar corona, the temperature exceeds 10^6 K so that some particles can escape the solar gravitational attraction. The stream of particles leaving the solar atmosphere is called the solar wind, which is mainly composed by electrons and protons (with about 10% alpha particles). This plasma travels the interplanetary space at supersonic speeds, between 400 km/s near the neutral surface of the heliosphere and 800 km/s near the coronal holes. The solar wind also transports the magnetic field of the Sun, forming the Interplanetary Magnetic Field (IMF).

2.1.3 Solar Activity Cycle

The Sun has activity following a cycle of approximately 11 years. The number of sunspots appearing on the surface of the Sun increases and decreases according to this periodic variation, as illustrated in Fig. 1. The years 2024-2025 correspond to a maximum of solar activity, so that strong events appeared during these years *[Pierrard et al., 2024, Pierrard et al., 2025b]*. The sunspots are generally source of active regions where solar eruptions originate. The period of 11 years corresponds to the time for the inversion of the magnetic North and South polarities of the Sun. The magnetic poles of the Sun return to the same direction with respect to a reference galactic orientation only after a second inversion of 11 years of activity. The full cycle of Hale thus lasts 22 years.

2.1.4 Magnetic environment of the Earth

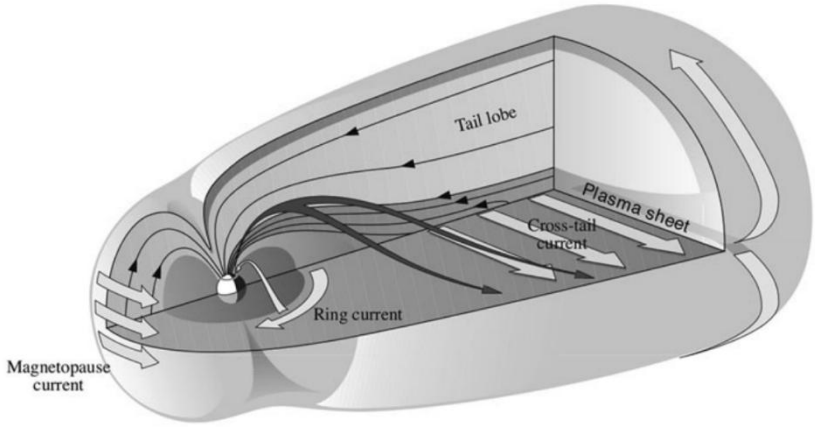

Figure 2: Magnetosphere of the Earth. Image from [Koskinen and Kilpua, 2022]

The magnetosphere of Earth results from the interaction of the geomagnetic field and the solar wind. The boundary between the space dominated by the IMF and the space dominated by the magnetic field of the Earth is called the magnetopause. On the day side of Earth, the magnetosphere is compressed inward to about 10 Earth radii (R_E) due to the pressure of the solar wind. The position of the magnetopause in the day side strongly depends on the condition of the solar wind and can be pushed back to geostationary distances to Earth (~ 6.6 R_E , with 1 R_E ≈ 6371 km) *[Koskinen and Kilpua, 2022]*. In the night side, the magnetosphere is stretched out up to 100 RE, creating the magnetotail. It is composed by two lobes of opposite magnetic polarity which are separated by the plasma sheet, composed by hot plasma of both solar and ionospheric origin *[Pierrard, 2009]*. This constitutes the outer magnetosphere.

The inner magnetosphere is the region where the magnetic field is quasi-dipolar. In this region, one finds a variety of particle species with various energies, as well as various spatial distributions:

1. The ring current is generated by the azimuthal drift motion of energetic particles. Electrons move in the eastward direction while positively charged particles move in the westward direction. The particles forming the ring current are located between 3-8 R_E from Earth *[Koskinen and Kilpua, 2022]*.

2. The radiation belts are mainly composed by high-energy electrons and protons trapped in the quasi dipolar geomagnetic field. A more detailed explanation of the belts is given in the next section.

3. The plasmasphere is the most inner part of the magnetosphere. It is composed of cold and dense plasma (~ 1 eV) originating from the ionosphere *[Pierrard et al., 2021a]*. The limit of the plasmasphere is relatively well defined by sharp drop in electron density and is called the plasmapause *[Koskinen and Kilpua, 2022]*.

All of those components of the inner magnetosphere spatially overlap and interact with each other. Specifically, the plasmapause, whose position strongly depends on the magnetic activity, plays an important role in the dynamics of the outer belt electrons.

2.1.5 The Van Allen radiation belts

The terrestrial radiation belts were discovered in 1958 by James Van Allen and his coworkers with the launch of the first American satellite Explorer 1. The spacecraft was equipped with a Geiger-Müller instrument whose goal was to measure cosmic radiation. The instrument worked well up to an altitude of 700 km where the count of the Geiger instrument suddenly dropped to zero. The satellite was traveling through a region where the

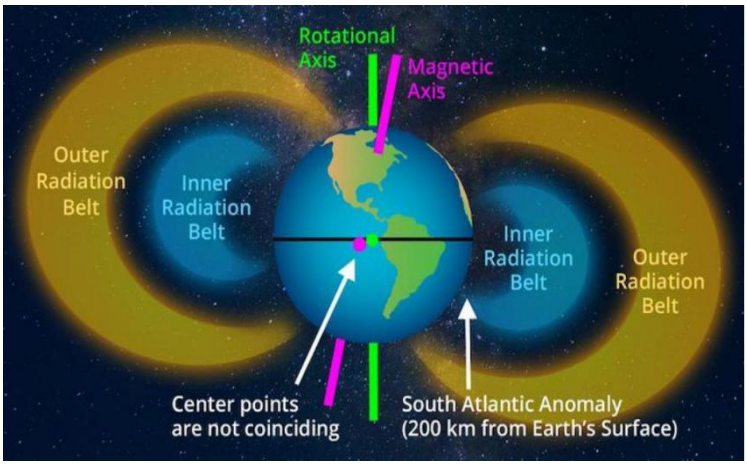

Figure 3: Schematic drawing of the Van Allen Radiation belts. The deeper penetration of the inner belt is also represented. This image was taken from https://stellariasacademy.online/south-atlantic-anomaly/20/05/

radiation was so intense that the instrument was saturated *[Pierrard, 2009]*. The radiation belts are toroidal regions populated by high-energy particles trapped in the magnetic field of the Earth. They mainly consist of electrons and protons (with a very small fraction of heavier ions). The energy range of the particles in the radiation belt is comprised between ~ 10 keV and ~ 1 MeV for the electrons and between ~ 100 keV and ~ 100 MeV for protons in the inner belt. There are two distinct radiation belts. The inner belt, located closer to Earth, extends up to 4 R_E in the equatorial plane. It is populated by both electrons and protons of varying energy. The outer belt, which extends from 4 R_E to 10 R_E in the equatorial plane, is composed in majority of electrons. This belt is much more variable in time than the inner one. The two belts are separated by a slot region, where the flux of particles is much lower. The position and width of the slot, as well as of the radiation belts, depend on the energy of the electrons *[Pierrard, 2009]*. It is also interesting to note that a configuration with three belts was observed during one month for ultrarelativistic electrons (E > 3.4 MeV) *[Koskinen and Kilpua, 2022]*. After the Mother's Day event on 11 May 2024, even 4 radiation belts were observed for the first time and during more than one month *[Pierrard et al., 2024]*.

2.1.6 South Atlantic anomaly

The geomagnetic field of the Earth is generated in its liquid core. The magnetic dipole axis is not aligned with the rotation axis: an angle of 11° separates them. In addition, the center of the dipole does not coincide with the center of gravity of Earth. The center of the dipole is 500 km away, toward the northern Pacific. Due to the combination of both offsets (in angle and in position), the intensity of the magnetic field is minimum over the South Atlantic. Moreover, the magnetic dipole axis is the axis of symmetry of the radiation belts. Thus, protons of the inner belt can penetrate deeper into the atmosphere above this region, which is called the South Atlantic Anomaly or SAA *[Lopez Rosson and Pierrard, 2017]*. In addition, at a given altitude, the intensity of energetic proton fluxes is much higher over the SAA, which can have an impact on LEO orbiting satellites *[Pierrard, 2009]*.

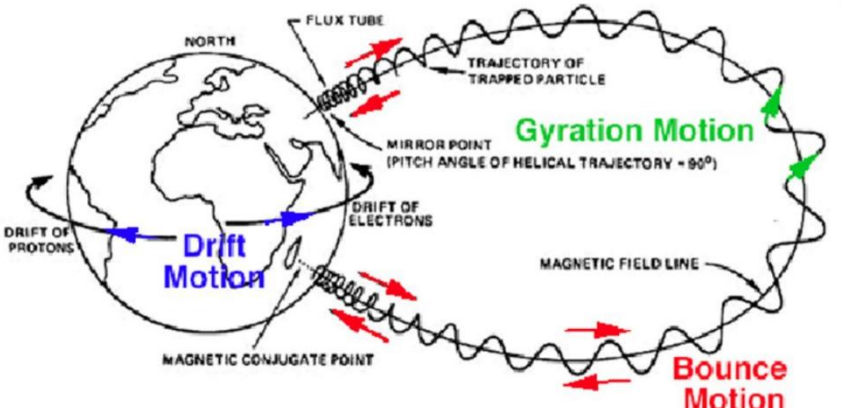

Figure 4: Representation of the superimposed motion of trapped particles in the radiation belts.

2.2 Motion of particles in the radiation belts

In the radiation belts, the plasma has a very low density, such that in good approximation, collisions between particles can be neglected and their motion is supposed to be independent from each other. The motion of charged particles is then driven by the Lorentz force acting on them, due to the presence of electric fields as well as geomagnetic field. The equation of motion of a given particle of mass m and charge q in the radiation belts is then given by:

$$m\boldsymbol{a} = q(\boldsymbol{E} + \boldsymbol{v} \wedge \boldsymbol{B}) + m\boldsymbol{g} \quad (1)$$

The solution of this equation is very complex, but can be obtained numerically. However, in order to better understand the movement of trapped particles, some approximations can be made. Their motion can be decomposed in three distinct (quasi-)periodic motions: the gyration motion around a guiding center, the bouncing motion along the magnetic field lines, and the azimuthal drift motion *[Pierrard, 2009]*.

2.2.1 Gyration motion

Considering a uniform and static magnetic field ***B*** pointing in the ***z*** direction, and neglecting other forces (like gravity and Coulomb force), the equation of motion of a non- relativistic charged particles of mass m and charge q is given by

$$m\frac{d\boldsymbol{p}}{dt} = q\boldsymbol{v} \wedge \boldsymbol{B} \tag{2}$$

The motion of the particle described by this equation can be split in two. First, the particle orbits a guiding center in the plane perpendicular to the magnetic field. Second, the movement of the guiding center parallel to the magnetic field *[Koskinen and Kilpua, 2022]*. From the circular motion, it is possible to derive the expression of the gyro radius (also called Larmor radius):

$$\rho_G = \frac{mv_\perp}{|q|B}, \tag{3}$$

where $v_\perp$ is the velocity perpendicular to the magnetic field. The gyro radius depends on the particle species, the energy as well as the intensity of the magnetic field. Thus, for a given particle which guiding center follows a given magnetic field line, its gyro radius is largest at the magnetic equator. The angular frequency of the gyration motion is given by the Larmor angular frequency:

$$\omega_G = \frac{v_\perp}{\rho_G} = \frac{|q|B}{m}, \tag{4}$$

and the Larmor period is thus:

$$T_G = \frac{2\pi}{\omega_G} = \frac{2\pi m}{|q|B} \tag{5}$$

2.2.2 Drift motion

Let us now consider the magnetic moment associated with the current created by the gyration motion of a particle around its guiding center. It can be defined as the ratio between the kinetic energy transverse to the magnetic field and the intensity of the magnetic field :

$$\mu_B = \frac{1}{2}\frac{mv_\perp^2}{B} \tag{6}$$

According to Faraday's law, the magnetic flux through the gyration loop of the particle is constant:

$$\phi = B\pi\rho_G^2 = \frac{2\pi m}{q^2}\mu_B = cst \tag{7}$$

Thus, μ_B is also conserved, and since the mass of the particle is constant,

$$\frac{v_\perp^2}{B} = cst \tag{8}$$

Due to conservation of the energy, and since $v^2 = v_\perp^2 + v_\parallel^2$, v is also conserved. The pitch angle of the particle is defined as the angle α such that $v_\perp = v \sin\alpha$. By the conservation of the magnetic moment and the definition of the pitch angle,

$$\frac{v^2 \sin^2\alpha}{B} = cst \tag{9}$$

Thus, for a given point at the equator and a point at higher latitude:

$$\frac{\sin^2\alpha_{eq}}{B_{eq}} = \frac{\sin^2\alpha}{B} \tag{10}$$

A particle moving from the equator (where the magnetic field is the weakest) to higher latitudes will see increasing intensities of the magnetic field. In order to satisfy the above relation, the pitch angle of the particle must also increase. This will be the case until the pitch angle value reaches 90°. At this point, all the energy of the particle is due to the perpendicular velocity (i.e $v_\parallel = 0$) and the particle cannot go to higher latitudes; it is called the mirror point. The particle will then move back toward the equator *[Pierrard, 2009]*. This bounce is caused by the mirror force, created by the gradient of the magnetic field, acting on the magnetic moment of the particle If s is the position of the guiding center along the magnetic field line and if s_m and s'_m are the coordinates of the mirror points, the bounce period is given by,

$$T_b = 2\int_{s'_m}^{s_m} \frac{ds}{v_\parallel(s)} = \frac{2}{v}\int_{s'_m}^{s_m} \left(1 - \frac{B(s)}{B_m}\right)^{-\frac{1}{2}} ds. \tag{11}$$

2.2.3 Bounce Motion

As mentioned in Equation 1, particles in the radiation belts are also affected by external forces. If the external forces are perpendicular to the magnetic field (homogeneous and stationary), the particle velocity can be decomposed into a gyration velocity (v_L) around the guiding center and a drift velocity of the guiding center ($\boldsymbol{v_D}$), such that $v = v_D + v_L$. From Equation 1, it is possible to show that the drift velocity is given by:

$$\boldsymbol{v_D} = \frac{\boldsymbol{F} \wedge \boldsymbol{B}}{qB^2}, \tag{12}$$

where F represents the external forces. The drift velocity is always perpendicular to the magnetic field and the force creating it. The azimuthal drifting motion of particles can lead to the production of electric current which current density is given by:

$$\boldsymbol{J} = ne(v_F^+ - v_F^-), \tag{13}$$

assuming quasi-neutrality of the plasma. Here is the list of forces that lead to the drift motion of particles and their contribution to the formation of an electric current,

1. Gravity: $F = mg$. In this case, positively and negatively charged particles drift in opposite directions. Electrons drift to the West, while positive ions drift to the East. The drift velocity is proportional to the mass of the particle and is thus much larger for ions than electrons. This produces an electric current that flows in the opposite directions than the observed ring current.

2. Coulomb force: $F = qE$. In the presence of an electric field, the drift velocity of all species is the same. It does not contribute to the formation of an electric current. In addition to that, if the electric field in the magnetosphere is equal to the co-rotating electric field F_{corr}, all particles will drift eastward with the same speed as the Earth's angular speed Ω_E. The co-rotating electric field is given by:

$$\boldsymbol{E_{corr}} = -(\boldsymbol{\Omega} \wedge \boldsymbol{r}) \wedge \boldsymbol{B} \tag{14}$$

3. Magnetic field gradient: $F = -\mu_B \nabla B$. This is the force applied by an inhomogeneous magnetic field on the magnetic dipole formed by the gyration motion of the particles. In this case, the drift velocity is proportional to the mass as well as the energy of the particles. In addition to that, the drift of electrons and ions has opposite directions, electrons drift in the eastward direction and positive ions in the westward direction.

$$\boldsymbol{v_B} = \frac{-\mu_B \boldsymbol{\nabla} B \wedge \boldsymbol{B}}{qB^2} \tag{15}$$

The guiding center approximation (i.e. the decomposition of the motion in the gyromotion and the motion of the guiding center) holds valid as long as the gyro radius of the particles is much smaller than the characteristic variation distance of the magnetic field, i.e.

$$\rho_G \ll \frac{B}{|\boldsymbol{\nabla} B|} \tag{16}$$

The guiding center approximation is also valid if the drift velocity is much smaller than the gyration velocity. For electrons and ions from 1 to 100 keV, the force due to magnetic field inhomogeneity is responsible for the creation of the ring current which in turn is responsible for the weakening of the geomagnetic field during magnetic storms.

4. Curvature of the magnetic field lines. The force in play here is the centrifugal force on the particle caused by the curvature of the field lines and is given by

$$\boldsymbol{F} = \frac{m v_\parallel^2}{R_c} \boldsymbol{n}, \tag{17}$$

where $R_c = \frac{B}{\nabla B}$ is the curvature radius of the magnetic force lines for rotational-less field and n is the normal unit vector of the field lines and directed outward. The drift speed of trapped particles thus becomes:

$$\boldsymbol{v_{R_c}} = -\frac{m v_\parallel^2 (\boldsymbol{\nabla} B)_\perp \wedge \boldsymbol{B}}{qB^3} \tag{18}$$

It is possible to combine the drift motion due to the magnetic force and the curvature of the field line to find and expression for the total drift velocity due the the magnetic field:

$$\boldsymbol{v_B} = \frac{m}{2qB^3} \left(v_\parallel^2 + v_\perp^2\right) \boldsymbol{B} \wedge \boldsymbol{\nabla} B \tag{19}$$

Thus, electrons drift to the eastward direction while protons and ions drift in the westward direction.

5. Inertial force. This force appears when the drift velocity of the guiding center is not constant,

Particle	ρ_g	T_g (s)	T_b(s)	T_D(min)
Electrons (1 MeV)	320 *m*	7 x 10^{-6}	0.1	50
Protons (10 MeV)	30 *km*	5 x 10^{-5}	0.65	3.2

Table 1: Typical numerical values for the gyration radius ρ_g, gyration period T_g, bounce period T_b and drift period T_D for electrons and protons of the radiation belts [Pierrard, 2009].

$$\boldsymbol{F} = -m\frac{d\boldsymbol{v_D}}{dt} \tag{20}$$

Thus, if the ambient fields are stationary, i.e $\frac{dE}{dt} = 0$ and$\frac{dB}{dt} = 0$, there is no variation in the drift velocity of the guiding center and thus $v_I = 0$. However, if the electric field is not stationary but the magnetic field is stationary, the variation in the drift velocity is only due to the variation of the drift velocity caused by the electric field: $\frac{dv_D}{dt} = \frac{dv_E}{dt}$. Then, the drift velocity due to the inertial force is given by

$$\boldsymbol{v_I} = -m\frac{\frac{d\boldsymbol{E}}{dt} \wedge \boldsymbol{B}}{B^2} \wedge \frac{\boldsymbol{B}}{qB^2} = m\frac{\frac{d\boldsymbol{E}}{dt}}{qB^2} \tag{21}$$

This drift motion is called the polarisation drift and the resulting electric currents are called polarisation currents. The total drift velocity of the trapped particles in the geomagnetic field is the sum of all the above mentioned velocities:

$$\boldsymbol{v_{tot}} = \boldsymbol{v_g} + \boldsymbol{v_E} + \boldsymbol{v_B} + \boldsymbol{v_I} \tag{22}$$

The importance of these components depends on the energy of the trapped particles, as well as the intensity and variability of the electric and magnetic field *[Pierrard, 2009]*.

2.3 Adiabatic Invariants

As described above, the motion of trapped particles in the radiation belts can be de- composed in three separate (quasi-)periodic motions. In the context of Hamiltonian mechanics, it is possible to show for quasi-periodic systems that if p is the canonical momentum and q is the canonical coordinates, the following quantity,

$$I = \frac{1}{2\pi}\oint \boldsymbol{p} \cdot d\boldsymbol{q}, \tag{23}$$

is an adiabatic invariant over the quasi-period *[Koskinen and Kilpua, 2022]* (a proof is given in *[Ukhorskiy and Sitnov, 2012]*). Such quantities are approximate constants of slowly varying systems (i.e., the variation time scale of the system is much larger than the period of the motion). To each (quasi-)periodic motion found in the belts, it is possible to associate an adiabatic invariant. However, in the belts, rapid variations of the magnetic field can lead to non-adiabatic motion (i.e. violation of the adiabatic invariants) of particles and significantly contributes to particle losses in the population of the belts.

2.3.1 The first adiabatic invariant

The first adiabatic invariant is associated with the gyromotion of trapped particles. If the guiding center approximation holds and for ρ_L the canonical coordinate and $p_\perp$ the canonical momentum,

$$I_1 = \frac{1}{2\pi}\oint \boldsymbol{p}_\perp \cdot d\boldsymbol{\rho_L} = \frac{1}{2\pi}\int_0^{2\pi\rho_L} m\, v_\perp dl = \frac{m}{q}\mu_B, \tag{24}$$

where $\mu_B = \frac{mv_\perp^2}{2B}$ is the magnetic moment, is an adiabatic invariant. Thus, the magnetic moment and the magnetic flux through the gyration loop ($\phi = \frac{2\pi m}{q^2}\mu_B$) are constants of the motion. As the particle evolves in the magnetic field, its gyration speed will increase as the magnetic field intensity rises in order to satisfy the conservation of μ_B . This acceleration is called the betatron acceleration *[Pierrard, 2009]*. In practice, this adiabatic invariant is less susceptible to be violated, since the gyromotion has the smallest period (see Table 1.1) which is almost always smaller than the characteristic time variation of the magnetic field.

2.3.2 The second adiabatic invariant

The second adiabatic invariant is linked to the bouncing motion of the particles between the two mirror points. In this case, the canonical coordinate is reduced to s, the position of the guiding center on the magnetic field line and the canonical momentum is reduced to the momentum parallel to the magnetic field $p_\parallel$. Thus,

$$I_2 = \frac{1}{2\pi}\oint p_\parallel\, ds = \frac{1}{2\pi}\oint m\, v_\parallel ds = cst \tag{25}$$

By definition of the pitch angle, $p_\parallel = p\cos\alpha$. For a particle at a mirror point, the pitch angle is equal to 90°, and the magnetic field line is given by B_m. By virtue of Equation 10, for all s

$$\frac{\sin^2\alpha\,(s)}{B(s)} = \frac{1}{B_m} \tag{26}$$

Thus, the parallel component of the momentum can be expressed as

$$p_\parallel(s) = p\sqrt{1-\sin^2\alpha\,(s)} = \sqrt{1-\frac{B(s)}{B_m}} \tag{27}$$

Injecting this expression in the integral above results in $I_2 = 2pI$, where

$$I = \int_{s'_m}^{s_m}\left(1-\frac{B(s)}{B_m}\right)^{\frac{1}{2}} ds \tag{28}$$

If the characteristic variation scale of the magnetic field is very large, the magnetic moment and the momentum are conserved and the integral I is constant. So, if the particle moves in a region where the intensity of the magnetic field is higher, the mirror points will be located at higher altitudes and thus, the distance travelled between the two mirror points will be smaller. In addition to that, with the conservation of the second adiabatic invariant, the velocity of the guiding center increases. This acceleration is called the Fermi acceleration *[Pierrard, 2009]*. The violation of the second invariant can occur in region where the variation of the field are fast on distances close to the curvature radius, where the field lines are stretched and when the characteristic time scale of variation of the field is smaller than the bounce period (given by Equation 11).

2.3.3 The third adiabatic invariant

The third and last adiabatic invariant is associated with the azimuthal drift motion of the trapped particles. It expresses the conservation of the magnetic flux in the loop formed by a 360° drift motion of the guiding center. It can be expressed as

$$I_3 = \frac{1}{2\pi}\oint \boldsymbol{A}\cdot d\boldsymbol{l}, \tag{29}$$

where A is the potential vector of the field and dl is the infinitesimal arc of the drift path of the guiding center *[Koskinen and Kilpua, 2022]*. It can also be written with the form

$$I_3 = \frac{1}{2\pi}\oint m\, v_D r d\phi, \tag{30}$$

where v_D is the drift velocity of the particles, ϕ the azimuthal angle and r the radius of the drift orbit of the particle. Because this last adiabatic invariant is associated to the drift motion which features the largest period, it is the one that is the most frequently violated. This can happen if the variation of the magnetic field is more rapid than the drift period. Wave-particle interactions with ultra-low frequency (ULF) oscillations of the magnetic field and small-scaled spatial variations of the magnetic field lead to the non-conservation of the third invariant. Those processes are involved in the non-adiabatic acceleration of electrons in the outer belt *[Pierrard, 2009]*.

2.4 Geomagnetic Coordinates *(B, L)*

Due to the motion of the particles trapped in the geomagnetic field of the Earth, it is often convenient to use the geomagnetic (B, L) coordinates. Those coordinates were introduced by McIlwain in 1961 *[McIlwain, 1961]* in order to solve the problem of mapping observed fluxes of energetic trapped particles. In this coordinate system, B is the intensity of the magnetic field at the point of measurement and *L* is the McIlwain parameter or the magnetic shell parameter. It gives, for a dipolar magnetic field, the distance at the equator of the magnetic shell of a trapped particle whose pitch angle is 90° at the point of measurement *[Pierrard, 2009]*. The shell parameter is useful because, by construction, it is constant along the magnetic field lines. Thus, each value of *L* uniquely defines a drift shell in which particles evolve.

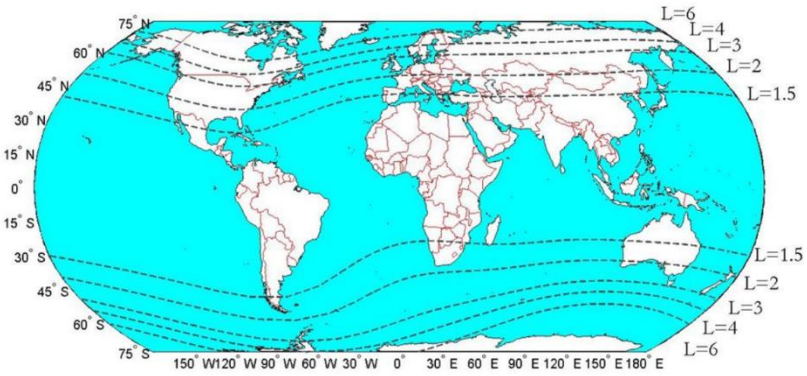

Figure 5: Constant L-shell projected on the surface of the Earth.

2.5 Physical processes in the radiation belts

The state of the radiation belts is determined by the balance between the sources of energetic particles and the loss processes affecting them. The difference in temporal, spatial, and flux intensity variability between the inner and outer belts indicates that the physical processes that occur in these regions are different. This is due to the fact that the inner and outer belts feature non-identical particle populations. In this section, a brief description of the main processes involved in both belts is presented.

2.5.1 Inner Belt

The inner belt is mostly populated by high-energy protons ranging from several MeV up to GeV. However, [*Pierrard et al., 2019*] showed that the inner belt also contains electrons with energy up to 1 MeV. It is very stable in relatively short periods of time and shows variability only during large solar energetic particle (SEP) events that are often, but not always, shortly followed by magnetic storms *[Pierrard et al., 2023]*. However, the inner belt varies in time with the solar activity cycle of 11 years. The residence time of protons in the inner belt

spreads from several years for proton whose pitch angle is close to the atmospheric loss cones, to several thousands of years for protons mirroring close to the equator *[Koskinen and Kilpua, 2022]*. There are two main sources of high-energy protons for the inner belt, cosmic rays and SEP events. When very high-energy protons collide with nitrogen or oxygen atoms of the terrestrial atmosphere, neutrons are produced by nuclear reactions. About 10% of the neutrons travel away from the Earth and decay into a proton and an electron. Those charged particles are then trapped in the magnetic field of Earth and form the inner radiation belt. If the source of the incoming proton is cosmic rays, this process is called cosmic ray albedo neutron decay (CRAND). However, if the primary proton originates from a strong SEP event, the above mentioned process is called solar proton albedo neutron decay (SPAND) *[Pierrard, 2009]*. Protons from SEP events that cannot penetrate the neutral atmosphere can be directly trapped in the inner belt at ~ L = 2−2.5 and then transported radially closer to Earth via radial diffusion. The loss mechanisms in the inner belts mainly consist of charge exchange and nuclear reactions with neutral atoms present in the exosphere. During a charge exchange, a highly energetic proton collides with a neutral atom, and an electron of the neutral atom is transferred to the proton. This leaves a relatively low-energy proton that remains trapped in the magnetic field and a very energetic atom that is no longer influenced by the electromagnetic fields surrounding the Earth. Nuclear reactions and Coulomb collisions with ionospheric and plasmaspheric ions contribute to the gradual slowing of protons *[Koskinen and Kilpua, 2022]*.

2.5.2 Anisotropic proton fluxes

One of the particularities of particle fluxes at low altitudes is that the high-energy trapped proton fluxes are strongly anisotropic, i.e., the proton fluxes depend on their arrival direction in the plane perpendicular to the local magnetic field vector as well as on their pitch angle (angle between their velocity vector and the local magnetic field vector). The anisotropy manifests itself through a steep pitch angle distribution and the so-called East-West effect. The pitch angle distribution is due to the particle gyration around magnetic field lines and their mirroring in an inhomogeneous magnetic field. The East-West asymmetry is caused by the finite size of the proton gyroradius and is the result of the interaction of the protons with the Earth's magnetosphere. Below 2000 km, the gyroradii of trapped protons with energies > 1 MeV are comparable to the neutral atmospheric scale height. The scale height represents the vertical distance above a planet's surface at which the density or the atmospheric pressure decreases by an exponential factor of e = 2.718. This means that during a gyration, the protons encounter different atmospheric densities, causing differences up to an order of magnitude for fluxes arriving from different azimuths.

Due to all those particularities mentioned above, studying proton fluxes at low altitudes and especially in the South Atlantic Anomaly is very complex. Many parameters need to be taken into account: proton energy, local position, pitch angle, East-West looking direction, solar activity level, solar cycle phase and external sporadic disturbances such as geomagnetic storms or solar energetic particle (SEP) events. When analysing high-energy proton data from instruments at LEO, it is important to take those parameters into account *[Pierrard et al., 2023]*.

2.5.3 Outer belt

The outer belt is populated by high-energy electrons and is much more variable in time than the inner belt *[Pierrard et al., 2020]*. The electron fluxes can vary in very short periods of time, and so does the spatial extent of the outer belt. The main sources of the outer belt electrons are the solar wind and the ionosphere. However, the energies of particles present in the solar wind (~ keV) and in the Earth ionosphere (~ eV) are much smaller than those for the radiation belt particles (~ MeV). There must exist some physical processes that allow the transport of electrons to the radiation belt and accelerate them to higher energies. If variations of the magnetic field occur on smaller time scales than the drift motion of the electrons, the violation of the conservation of the third adiabatic invariant causes radial drift motion in the belts. In addition, electrons from the radiation belts interact with plasmaspheric waves that are found in the plasmasphere *[Pierrard et al., 2021b]*. Wave-particle interactions have various affects on electron populations, such as radial diffusion (interactions with ULF waves) and accelerations (interactions with ULF waves, Whistler-Mode chorus waves) *[Dahmen et al., 2022]*. Losses of energetic electrons in the outer belt can occur through "real" loss of electrons to the magnetopause or the atmosphere, or can be decelerated to very low energy, thus becoming part of the background plasma. One way that leads to electron losses is the so- called magnetopause shadowing. If electrons of the outer belt can cross the magnetopause, they are no longer trapped in the Earth's magnetic field and are lost in interplanetary

space. The crossing of the outer belt drift shells and the magnetopause has various origins, mainly the drift shell radial expansion during the main phase of magnetic storms and the compression of the magnetopause in the radiation belts *[Koskinen and Kilpua, 2022]*. An other sink for the outer belt electrons is the precipitation in the atmosphere. Interactions between plasmaspheric waves and particles cause pitch-angle scattering of the electrons in the atmospheric loss cone, i.e. modify the pitch angle so that the mirror point of the electrons is located in the atmosphere and they are lost through collisions. Energy scattering of electrons is also possible due to wave-particle interactions with various plasma waves found inside and outside the plasmasphere. After being decelerated, the electrons become part of the low-energy plasma background *[Koskinen and Kilpua, 2022]*.

2.6 Geomagnetic storms

Magnetic or geomagnetic storms are periods during which the magnetic field in the magnetosphere and near the Earth is strongly perturbed. Although not unique, the most common planetary index used to detect magnetic storms is the disturbance storm time index (Dst). This index characterizes the intensity of the horizontal component of the magnetic field at the surface of the Earth in equatorial regions. During a storm, the horizontal component of the magnetic field at the surface decreases. This is due to the intensification of the equatorial ring current, which tends to reduce the intensity of the geomagnetic field *[Pierrard, 2009]*. Stormy episodes are distinguished in the Dst time series by inverted peaks. There is no fixed threshold in the Dst that marks a magnetic storm. However, the value of −50 nT is often used as a lower limit for moderate storms *[Koskinen, 2011]*. The time extent of geomagnetic storms is between several hours and several days. It corresponds to the time necessary to decrease the current density of the ring current by reducing the energy of ions and electrons that it contains but also by lowering its density through precipitation into the atmosphere *[Pierrard, 2009]*.

A geomagnetic storm unfolds in 3 phases,

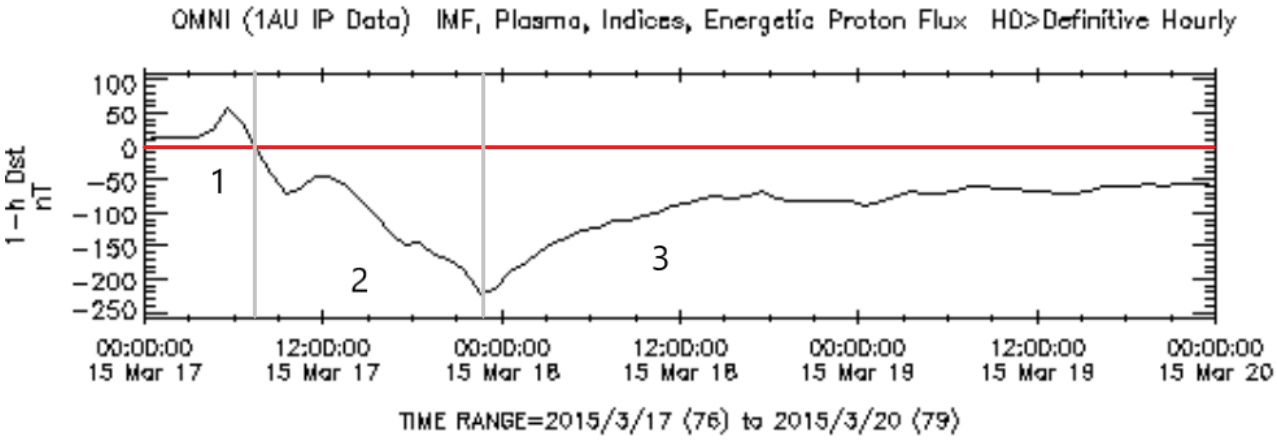

Figure 6: Evolution of the Dst index during the storm of March 17, 2015. The red line shows the constant zero value of the Dst. The different numbers correspond to the phases of the magnetic storm. 1. The initial phase with a sudden commencement (SC). 2. The main phase of the storm. 3. The recovery phase. This image has been generated on the NASA website: https://cdaweb.gsfc.nasa.go/index.html

1. The initial phase differs between storms. The length of the initial phase depends on the structure of the solar wind that drives the storm. If the IMF is directed southward, the initial phase is very short and the main phase of the storm is almost immediate. Some storms also begin with sudden commencements (SC), i.e a sudden increase in the Dst index before the main phase (see Fig. 6). This commencement is due to the solar wind shock wave hitting the magnetopause *[Koskinen, 2011]*.

2. The main phase is the period during which the horizontal component of the magnetic field and thus the Dst index reaches a minimum value. It is caused by the increase in density of the ring current as well as the acceleration of the particles forming it by the solar wind.

3. The recovery phase begins when the input of energy and particles of the solar wind come to an end. The time spread of the recovery phase is much larger than for the main phase, it can last several days. The reason for such a gap in the main and recovery phase time scales is that the physical processes leading to the loss of energetic particles in the ring current are much slower than during the injections.

Magnetic storm formation often occurs when the IMF has a strong southward component for a relatively long period of time (~3 h) *[Koskinen, 2011]*. Several phenomena can fulfill those conditions, such as fast solar wind or more extreme events like Solar Energetic Particle events (SEP). SEP events are characterized by the large flux increase of electrons, protons, and heavier ions to energies much higher than average. In some very extreme events, the protons energies can reach GeV *[Klein and Dalla, 2017]*.

3 Satellite flux data analysis

3.1 Open source data

In space physics, satellite data are often provided in open access to any interested scientist. When using such data, it is important to contact the Principal Investigator (PI) of the instrument to make sure to properly analyze validated and appropriate data. The team that has developed the instrument can provide more detailed information on contamination or data quality. This can complete the data information generally provided at the source that allows us to take into account the levels of data (how they have been transformed) and provide the quality flag indicating the relevance of each measurement. In the following, we will illustrate the data analysis by using the observations of a detector developed by BIRA-IASB with the University Catholique de Louvain and Redwire Space: the Energetic Particle Telescope (EPT) instrument *[Pierrard et al., 2014]*. This instrument was launched onboard the European Space Agency PROBA-V satellite in May 2013 on a Low Earth Orbit at 820 km. The EPT discriminates between electrons, protons and helium ions in energy ranges 0.5-20 MeV, 9.5-300 MeV and 38-1200 MeV, respectively.

3.2 Differential flux and integral flux

The crucial quantity needed for the study of the radiation belts is the flux of trapped and/or precipitating particles. This flux is measured in situ by spectrometers or particle telescopes on board satellites, each with distinct orbits that explore various regions of the radiation belts. Despite differences in measurement techniques and satellite orbits, these instruments primarily yield a similar data product: particle flux (J). This encompasses electrons and protons, providing observations at specific points in space. It is essential to differentiate between the differential flux and the integral flux which are omnipresent in the data products. Onboard spectrometers and particle telescopes measure particle flux within specific energy channels, with the flux in a given channel referred to as the differential flux and expressed in [$cm^{-2}s^{-1}sr^{-1}MeV^{-1}$]. Typically, data products are presented as differential flux, along with the energy range of the channel in which they are measured. However, there are instances where only the integral flux is provided. In such cases, it represents the flux of all particles measured above a specified energy threshold, often applicable to protons for characterizing Solar Energetic Particle events. The omnidirectional integral flux is expressed in [$cm^{-2}s^{-1}$]. The integral flux is easily retrieved given the differential flux. Strictly speaking, we integrate the differential flux with respect to the energy and on all solid angles. In practice, we proceed to the following sum:

$$J_{int}(E > E_0) = 4\pi \sum_{i=0}^{N} J_{diff}(E_i)\ \Delta E_i, \tag{31}$$

where $J_{diff}(E_i)$ is the differential flux measured in the energy bin i and ΔE_i is the width of the channel i. Thus, the integral flux does not depend on the energy anymore, although it depends on the lowest energy threshold (E_0).

3.3 Displaying data

In most cases, data products include more than just differential or integral fluxes. Alongside the time of measurements, the spacecraft's position, intensity of magnetic field com- ponents, McIlwain parameter values, and other pertinent parameters for radiation belt studies are commonly provided. It is important to note that these parameters can vary between data products, often due to differences in satellite orbits or the aim of missions. The most straightforward method to represent particle fluxes is by plotting the flux time series for the relevant channel (if using the differential flux). Although this approach is the simplest for visualizing the evolution of particle fluxes in the radiation belts, it may offer limited insights into RBs dynamics. This method could be used to identify events characterized by significant increases or decreases.

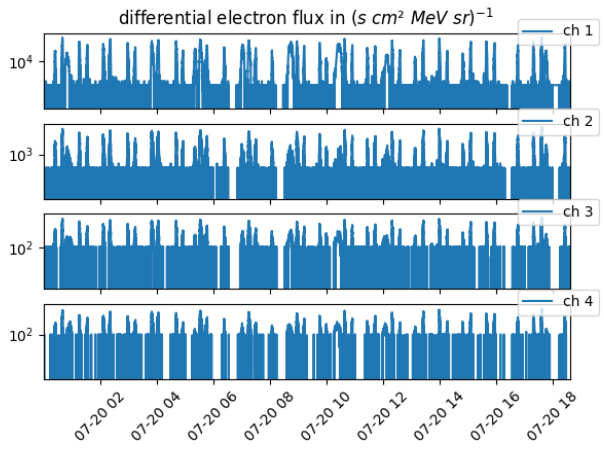

Figure 7: Electron differential flux measured by the Energetic Particle Telescope (EPT) on board the satellite PROBA-V [Pierrard et al., 2014] in 4 energy channels. ch1: 0.5-0.6 MeV, ch2: 0.6-0.7 MeV, ch3: 0.7-0.8 MeV, and ch4: 0.8-1.0 MeV.

The reason why plotting flux time series is not the most convenient way to visualize the data is that the location of measurements also varies in time. In fact, the satellites along their orbit pass through different regions of the RB, which feature different flux intensities. For example, the electron RBs feature a slot region, where the flux decreases sharply throughout the entire energy spectrum between the outer and inner belts. As the orbit of the satellite crosses this depleted region, the electron flux in the time series suddenly drops. Thus, flux variations in the most simple time series of the dynamics of the RBs are often more difficult to analyse.

It is much more useful to plot flux time series at "fixed" locations of the RBs. In order to do so, the McIlwain parameter L, which is constructed from a quasi-invariant of the motion of trapped particles, can be used. The most common way to represent RBs particle fluxes is to plot the flux as a function of both time and *L* as shown in Fig. 9. This way of displaying has the advantage of showing the evolution in time of the flux along each magnetic shells (labelled by *L*) on which trapped particles move. With this method, the entire structure of the RBs can be easily observed. In the figure, both the inner and outer belts can be clearly observed at *L = [1, 2.5]* and *L = [3.5, 8]* respectively. In the range *L = [2.5, 3.5]* the region depleted of electrons, called the slot, can be observed. From this figure, the dynamics of the radiation belts can be studied.

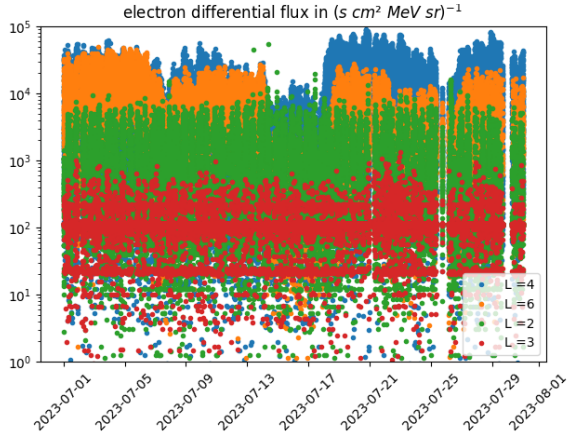

Figure 8: Electron differential flux measured by the Energetic Particle Telescope (EPT) in the first energy channel (0.5-0.6 MeV) at different values of L.

This figure illustrates well the issue that was mentioned earlier with plotting the data as simple flux time series. Indeed, it appears clearly now that as the instrument's position varies in space, the magnetic shell on which the flux of particles is measured also changes. Hence if the satellite crosses the slot region through its orbit, the flux sharply decreases in a small amount of time. Differentiating true variation of the flux or an effect of the satellite orbit is not an easy task to do if the McIlwain parameter (or another invariant quantity of the trapped particles' motion) is used to identify which region of the belts is probed.

As mentioned above, the parameters provided in the data products can differ from each other. Some parameters offer various ways to explore the data and study the RBs, which cannot be shown in this guide. However, if the satellite carrying the instrument is on a Low Earth Orbit (LEO), the longitude and latitude of the satellite are often provided along with the data. This allows us to create maps of the radiation belts and study their spatial distribution as shown in Fig. 10. In this case, for electrons, the three major regions of the RBs are also visible. The narrow bands of intense fluxes at high latitude in both hemispheres are the electron fluxes of the outer belt. The outer belt can be observed in both hemispheres because of the topology of the magnetic field and the oscillation motion of trapped particles along the magnetic field lines. The inner radiation belt can be observed on the map above the South Atlantic, where the electron fluxes are also high. At the altitude at which the EPT is in orbit, at ~ 820 km, the inner belt can only be observed over the South Atlantic due to the South Atlantic Anomaly, a region where the intensity of the Earth's geomagnetic field is lower than anywhere else. Due to the weaker magnetic intensity, trapped particles are able to penetrate at lower altitudes. Of course, the inner belt also exists at other longitudes, but at higher altitudes. The slot region on the map corresponds to the latitudes between the southern edge of the SAA and northern edge of the outer belt in the southern hemisphere.

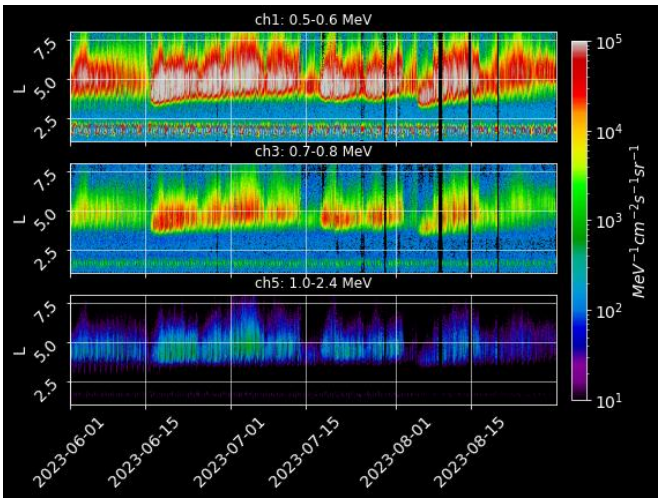

Figure 9: Electron differential flux as a function of L and time, as measured in the first three channels of the EPT during the first measurement campaign of the EURAMET BIOSPHERE project [Pierrard et al., 2025a], from June 1st 2023 to August 31st 2023. The channel energy width are the following; ch1: 0.5-0.6 MeV, ch3: 0.7-0.8 MeV

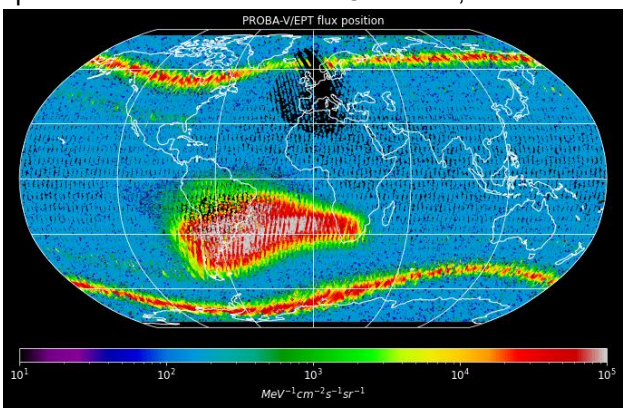

Figure 10: Map of the electron differential fluxes measured by the EPT in the first energy channel (0.5-0.6 MeV) during the first measurement campaign of the EURAMET BIOSPHERE project, from June 1st 2023 to August 31st 2023.

Representing the data in this way is convenient because it is easy to interpret. However, it is important to keep in mind that a large amount of data is needed to produce this kind of figure. Indeed, in Fig. 10, three months of observations from the EPT have been used. Because LEO satellites have a short orbit period (101 min. for PROBA-V *[Pierrard et al., 2014]*) and geomagnetic storms occur over the course of a few hours, visualizing the changes in the RBs dynamics on a map is not convenient. The method is particularly suited to study the long-term variations of the belts.

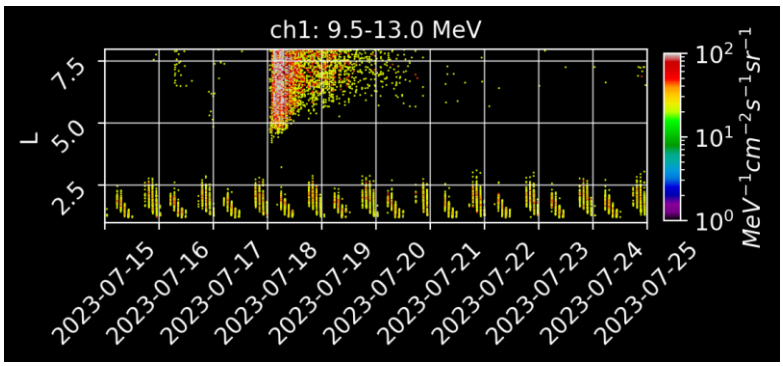

Figure 11: Differential proton flux measured by the EPT in the first energy channel during a SEP event in July 2023.

3.4 Data contamination and data quality

Instruments dedicated to accurately measuring RB fluxes can differentiate between particle types and resolve their energy spectra. However, the harsh RB environment implies potential data contamination. Contamination may arise from other types of energetic particles in the vicinity, particularly in the inner radiation belt, where electrons and protons coexist. In such cases, some protons may be misinterpreted as high-energy electrons, which introduces inaccuracies in the data. Another source of

contamination occurs when particles outside the instruments' field of view strike the detector. The calibration of the instrument and data quality flags are thus very important *[Cyamukungu et al., 2014]*.

As an example, Fig. 11 illustrates the EPT observations of solar protons injected at high L values during a Solar Energetic Particle (SEP) event that took place in July 2023. The protons trapped continuously in the inner belt are visible at lower L. Fig. 12 shows the EPT fluxes of electrons measured simultaneously. The top panel shows the unfiltered data, and the bottom panel the data filtered according to the quality flags of the data product. The protons of high energy are sometimes recorded by the instrument as lower energy electrons, causing the seemingly high electron fluxes at high L. However, the data quality flags provided in the EPT data product label those measurements as contaminated and must be removed from the data for radiation belt analyses.

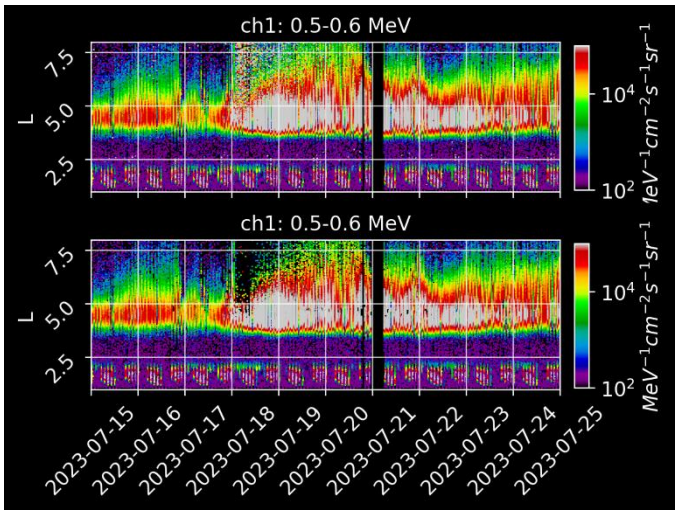

Figure 12: Top: Unfiltered electron differential flux observed by the EPT during a SEP event in July 2023. Contamination by protons is present in the outer belt. Bottom: Filtered electron differential flux observed by the EPT during the same SEP event in July 2023. Contamination by energetic protons has been removed

Due to these potential sources of contamination, data products often include indicators of data quality, such as quality flags, to convey the confidence level in the data. Understanding how these flags should be used is crucial, as misuse can significantly impact investigation results. Quality flags are typically provided by the instrument development team, and their interpretation may vary between data products. It is highly recommended to contact the Principal Investigator (PI) of the instruments to ensure accurate use and prevent errors when working with the data.

3.5 Averaging the data in time

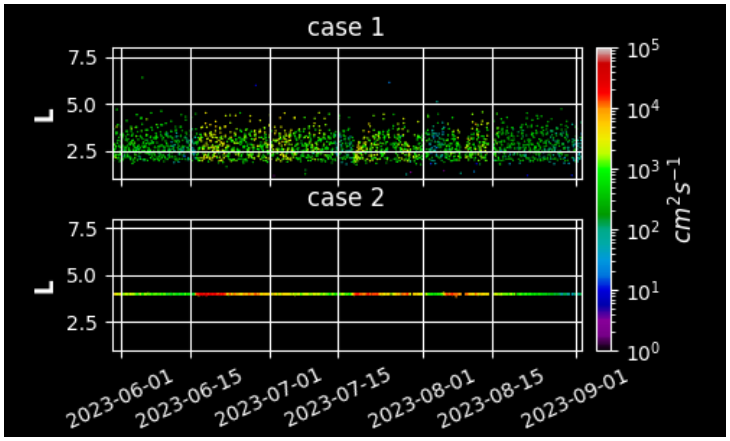

Figure 13: This figure shows the flux as a function of time and L, the McIlwain parameter for two different ways to average the data. Case 1 (top) Averaging EPT data on time before setting a L shell. Case 2 (bottom) Setting L = 4 ± 0.25 before averaging on time.

Onboard spectrometers and particles telescopes can measure particle fluxes with a very high resolution, for example, the EPT records the flux every 2s. This is of course very useful, but it also leads to a very large amount of data, and in some cases, such a high resolution is not needed (normalizing data for a prediction model, comparing observations from different instruments, ...). Then, it makes sense to average the data over longer periods of time. However, performing time averages is not as straightforward as taking all the data and averaging the flux over the desired time interval. The reason for this is again the time-dependent position of the observation location. The problem here is that if we simply take the time average of all the measurements and parameters provided in the data product, all the positions at which the instrument measured the flux during the given time span would also be averaged. Since the structure of the RBs is such that some regions feature higher fluxes than others, averaging the location of the instrument would lead to large errors in the averaged fluxes and in any position-dependent parameters. Of course, the error will be proportional to the time span in which the average is performed. If the data is averaged every minute, errors on the position of the instrument and thus on the flux will likely be negligible. However, if the time window for the average is one hour or even a day, simple averaging of the data is pointless. It is important to keep in mind that this source of error is also highly dependent on the orbit of the instrument carrier.

Considering that this issue is caused by the time-dependent position of the observation site, satellites that frequently traverse the different regions of the RBs are more susceptible to this source of error through the time average. For example, the Geostationary Operational Environmental Satellite (GOES) is in geostationary orbit, at $L \sim 6.6$, and always makes measurements in the outer radiation belts on magnetic shells that are close to each other. In contrast, PROBA-V/EPT *[Pierrard et al., 2014]* is on a heliosynchronous LEO orbit at an altitude of ~ 820 km. With this orbit, the satellite revolves around the Earth in approximately 101 minutes, rapidly crossing all magnetic shells and thus measuring fluxes in all three different RBs regions. The workaround to this difficulty is to set the location of the observations and then average in time the data that were observed at this location.

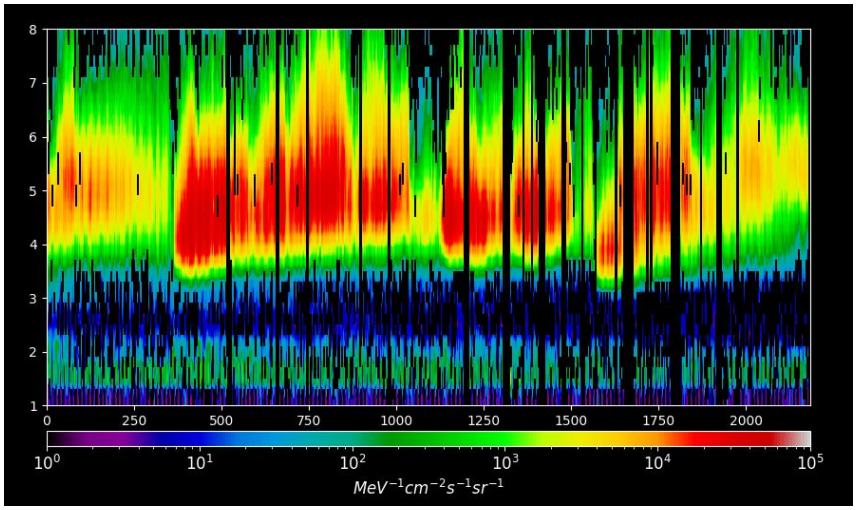

Figure 14: Hourly-averaged electron differential flux of the EPT in the first energy channel between June 1st 2023 and August 31st 2023.

In most cases, the parameter to use to set an observation location in the RBs is the McIlwain parameter or an equivalent parameter. Fixing a value of L will ensure that all measurements of particle fluxes occur on the same magnetic shell. However, depending on the averaging time span and the amount of available date, a larger/smaller area around the target L value must be defined to ensure that the average flux is statistically relevant. As an example of how simply averaging the data can affect the flux and the other parameters, Fig. 13 uses data from the EPT measured during the first measurement campaign of the EURAMET BIOSPHERE project, plotted as a function of time and L. This figure shows the 'wrong/naive' and the 'good' approach to average the data. In this example, the data are averaged over one hour. The top panel of Fig. 13 shows the hourly averaged electron flux in the first energy channel (0.5-0.6 MeV) as a function of time and L. Note that this panel actually is a simple hour average of Fig. 9. The structure of the RBs has completely disappeared, all measurements are located between $L = 2$ and $L = 5$. Also, the averaged flux intensity is significantly lower than that observed with the high resolution. What happens here, in the case of the EPT, is that the averaging period that was chosen is about half of the orbit period of the instrument. So, the top panel of Fig. 13 shows the measured average flux and the average L value of the EPT over half of its orbit, which is not representative at all of the actual hourly average flux in the radiation belts. In the bottom panel of the figure, only the data observed between $L = 3.75$ and $L = 4.25$ were averaged.

Fig. 14 shows EPT data from the first measurement campaign hourly averaged in L bins of width 0.2 L. It appears clearly that first setting a bin of L in which the data are averaged on time allows us to preserve the structure and the flux intensities that were observed in the high-resolution data. Here, the example has been presented with the McIlwain parameter. However, the same issue will arise with any position-dependent parameter (e.g., the longitude and latitude in the case of averaging the flux on a map). The same method should then be applied to those parameters.

3.6 The effects of the event of May 2024

On May 11th 2024, an extreme geomagnetic storm took place. This storm, which reached a minimum Dst value of -412 nT, is actually the most intense storm that was observed since the famous Halloween event of October 2003. It was caused by the arrival at Earth of several Coronal Mass Ejection (CMEs) that merged together. While the event unfolded, the EPT measured the flux of both energetic protons and electrons in the radiation

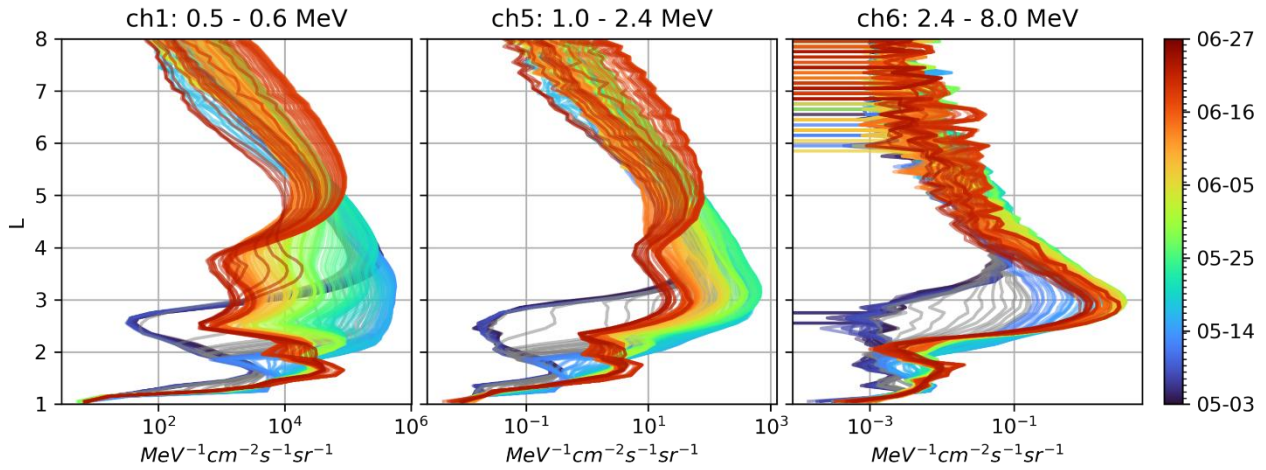

Figure 15: EPT smoothed electron differential fluxes as a function of L and time (color bar) in 3 different energy channels from 3 May to 27 June 2024. Greyed profiles correspond to the period between 8 and 10 May where the smoothed fluxes significantly deviate from the 6h averaged fluxes.

belts. The observations of the EPT, which are presented in details in *[Pierrard et al., 2024]*, revealed yet unseen dynamic responses of the proton and electron radiation belts to this extreme event. In the case of protons which are not shown here, the EPT showed a direct injection of protons from the outer belt into the inner belt. However, the injection only occurred in the South part of the SAA.. The smoothed electron differential flux profiles as a function of L and time are shown in Fig. 15. (i.e Fig. 9 in *[Pierrard et al., 2024]*). This figure reveals that after the main phase of the geomagnetic storm, very energetic electrons (with energies above 2.4 MeV) were also directly injected into the inner radiation belt. This behaviour of ultra-relativistic electrons was believed to be impossible based on the observations of the Van Allen Probes (VAPs) *[Baker et al., 2014]*. Moreover, during and after the recovery phase of the storm, the electrons that were injected in the radiation belts gradually decreases. In most cases, the recovery takes a few days and the two belts structure is reformed. In the case of the May 11th geomagnetic storm, the fluxes of electrons also gradually decrease. However, after several weeks, the flux of electrons in the slot region is still not reaching the pre-storm level. Moreover, the rate at which the electron flux decreases of is not constant in L and in energy. This leads to the formation of a multi-belts structure. For the first time, four belts were observed and last during more than one month after the event.

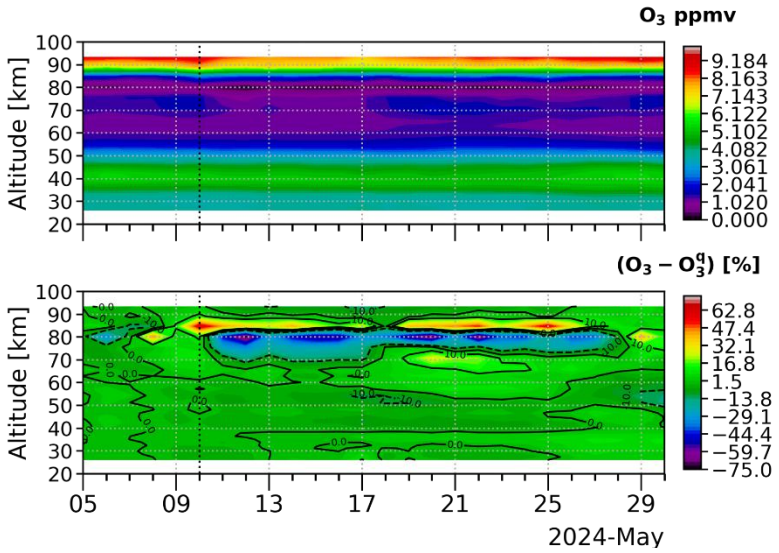

Figure 16: Evolution of atmospheric ozone during the month of May 2024 as a function of altitude. The top panel shows the ozone concentration in ppmv while the bottom panel show the relative difference in %

In addition to the radiation belts, this extreme geomagnetic storm greatly disturbed the ionosphere and the plasmasphere. *[Pierrard et al., 2025b]* have shown that following an increase of electron density during the main phase of the storm, the electron density was decreased for at least one day in comparison to the average during the 5 previous days.. This drop in ionization was not only caused by the loss of electrons in the F2 layer, but also to the strong

erosion of the plamasphere. Finally, the solar protons from the CMEs that caused the geomagnetic storm penetrated the upper atmosphere of the Earth. As they deposit their energy in the atmosphere, the flux of protons leads to an increase of the ionization rate at high altitudes. Changing the ionization rates can locally change the chemistry of the atmosphere. Fig. 16 shows the daily averaged observations of ozone from the MLS/Aura satellite over the southern polar hemisphere throughout the month of May 2024. This figure shows that just after the storm, as the ionization rate is increased, ozone is lost in the mesosphere at around 75 km of altitude (more details can be found in *[Winant et al., 2025]*).

3.7 Prediction of terrestrial radiation belts using deep learning

A prototype of a Neural Network model has been developed at BIRA-IASB to investigate and forecast the behaviour of near-Earth high-energy particles trapped in the Earth's magnetic field *[Botek et al., 2023]*. The model is driven by satellite data from the Energetic Particle Telescope (EPT) instrument *[Pierrard et al., 2014]*. The high spatial and time resolution of the measurements during more than 11 years represents an extraordinary coverage of quiet and stormy solar activity periods. These long-term observations allow for the successful training of a robust prediction model capable of very good performances from 1 to 8 L-shells ranges, where L is the equatorial distance of the magnetic field lines. The results of the model are the predictions of the logarithm of electron fluxes for two energy channels: 550 keV and 1.7 MeV.

4 Geant4 AtRIS simulations of energetic particle interactions with the atmosphere

4.1 What is the Atmospheric Radiation Interaction Simulator (AtRIS) ?

The propagation of high-energy particles through the atmosphere can be investigated with analytical models or with numerical models. The Atmospheric Radiation Interaction Simulator (AtRIS) *[Banjac et al., 2019a, Banjac et al., 2019b]* is an application based on GEometry ANd Tracking (GEANT4), a Monte Carlo simulation toolkit developed by the Central European Research Network (CERN) *[Agostinelli et al., 2003, Allison et al., 2006, Allison et al., 2016, Ivanchenko et al., 2011]*. In AtRIS, primary particles are injected one by one through a 3D spherical model of the atmosphere. After being injected into the atmosphere, primary particles are propagated through all layers of the atmosphere by GEANT4 in a step-by-step process.

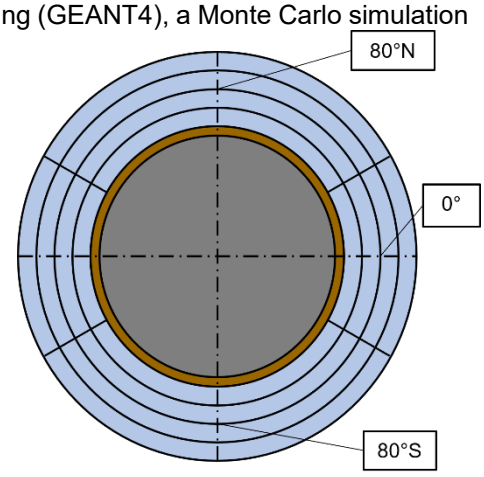

Figure 17: Sketch of the planet model described by a PSF used in [Winant et al., 2023]. In this model, the atmosphere is split into 3 regions with unique atmospheric properties.

4.2 Setting up a simulation

After both GEANT4 and AtRIS have been installed correctly, it is possible to run simulations. In order to run AtRIS, the entire simulation must first be set up properly, and some files are mandatory, for instance the Planet Specification File (PSF) which must be converted into a GDML file, the primary particle energy spectra and the phantoms that must be used to retrieve the radiation dose and count rates.

4.2.1 Creating the planet

The first step in setting up a simulation is to create a model of the planet and the atmosphere through which the primary radiation is going to be propagated. Every element of the planet and its atmosphere is defined in the Planet Specification File (PSF). Each row of the file corresponds to an element of the simulation. Each column of the file corresponds to a specific parameter that describes the said element. The number of columns in the PSF is variable, depending on the composition of the atmosphere. Once the planet was created in the PSF, the file is converted to a GDML file that can be read by AtRIS. In the case of the Earth, atmospheric properties and composition are computed with the NRLMSISE-00 or NRLMSISE-02 models *[Picone et al., 2002]*.

4.2.2 Providing the radiation phantoms

Phantoms are only needed for the computations of the dose rates in the atmosphere; however, even if one is only interested in the ionization, a phantom must be chosen for the AtRIS simulation to run. It is advised to use only the ICRU phantoms.

4.2.3 Providing the primary particle energy binning

Before running the simulation with AtRIS, the energy of the particles that are going to be injected into the atmosphere must be given to AtRIS. All that needs to be provided are the edges of the energy bins from which primary particles are injected at the top of the atmosphere in the simulation.

4.3 How to use AtRIS results ?

4.3.1 Ionization and dose rates

There are two main results from a simulation with AtRIS: the ionization and dose Atmospheric Response Matrices (ARMs). Those matrices describe the relation between the primary particle energy and the altitude-dependent average ionization and radiation dose in the atmosphere, respectively. The units of the ionization ARM are in [eV cm^{-3}] and [µGy] for the dose ARM. Examples of such matrices are shown in Fig. 18 for atmospheric ionization. Those matrices were computed using an atmosphere model similar to the one displayed in Fig. 17.

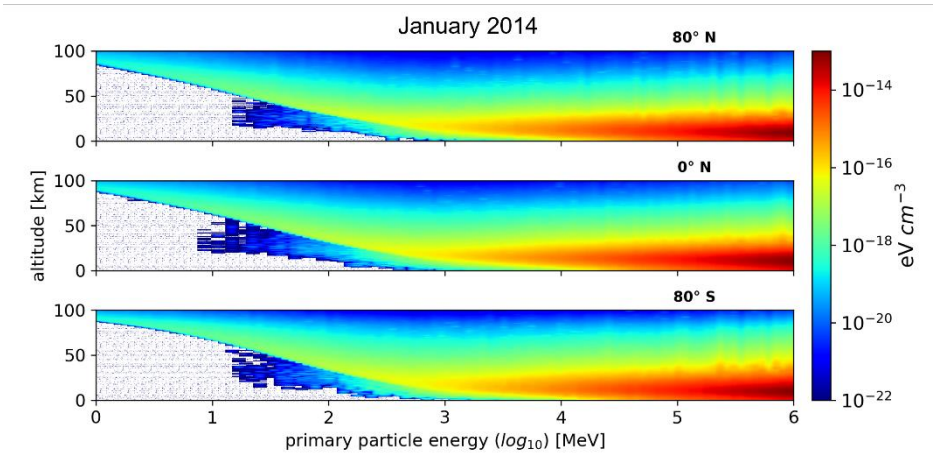

Figure 18: Ionization Atmospheric Response Matrices computed with AtRIS and the setup shown in Fig. 17.

The x-axis of the matrix is the energy of the primary particles (in MeV) corresponding to the energy binning that served as an input to AtRIS. The y-axis is the altitude. It depends on the model of the atmosphere and thus on the PSF. In Fig. 18, the atmosphere ranges from 0 km to 100 km and is divided into

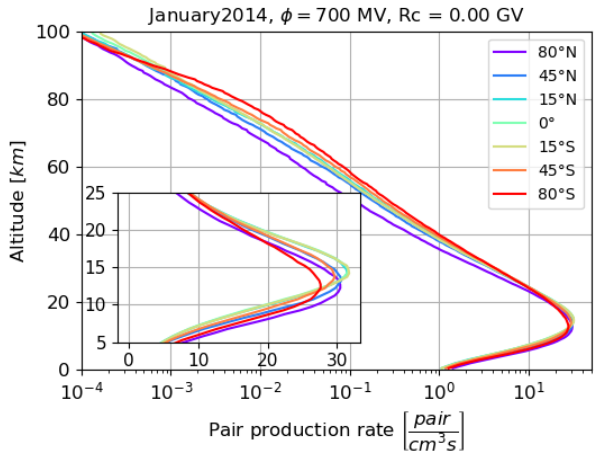

Figure 19: Ionization rates profiles in [pairs/cm^{3}s] computed with atmospheric response matrices at different latitudes [Winant et al., 2023]

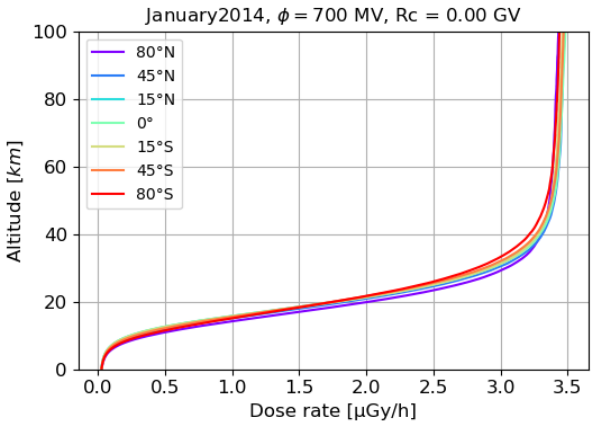

Figure 20: Absorbed dose rates profiles in [µGy/h] computed with atmospheric response matrices at different latitudes [Winant et al., 2023]

200 layers (each with a thickness of 500 m). The energy of the primary particles ranges from 10^0 MeV to 10^6 MeV divided into 100 bins.

The ARMs, which result from the AtRIS run, thus give the average response of the atmosphere at a given altitude (in a given layer) to a penetrating particle of a given energy (energy in a given bin). Thus, they do not give a representation of the real ionization or radiation dose in the atmosphere by themselves. In order to compute the realistic ionization or dose rate profiles in the atmosphere, we must provide a flux of primary particles precipitating in the atmosphere. In the case of solar energetic protons or radiation belt electrons, spectra can be obtained from EPT measurements or by fitting measurements from other detectors. Ionization rate results of AtRIS simulations obtained due to the penetration of particle fluxes of different energies in the terrestrial atmosphere are provided in *[Pierrard et al., 2025a]* for maximum and minimum solar activity. In the case of GCRs, primary particle flux at the Top Of the Atmosphere (TOA) is computed using the solution of the force-field approximation to solve the transport equation of charged particles through the heliosphere introduced by Parker:

partilce	code
photons	22
pions+	211
pions-	-211
kaons+	321
kaons-	-321
kaons0	310
electrons-	11
positrons+	-11
muons-	13
muons+	-13
protons+	2212
protons-	-2212
neutrons	2112
anti-neutrons	-2112
deutron	1000010020
triton	1000010030
helium3	1000020030
alpha	1000020040

Figure 21: List of particles created in AtRIS alongside with their respective PDGC code

$$\frac{dJ}{dE}(E,\Phi) = J_{LIS}(E+\Phi)\frac{E(E+\Phi)}{(E+\Phi)(E+\Phi+2E_r)}, \quad (32)$$

where $J_{LIS}(E)$ is the differential Local Interstellar Spectrum (LIS) of primary particles before they interact with the heliosphere, E_r is the rest energy, and $\Phi = (Ze/A)\phi(t)$ is the solar modulation function with Z the electric charge, e the charge of the electron, A is the atomic number and ϕ is the modulation potential. The solution of the equation allows to describe the differential flux of GCRs at 1 AU with only one free parameter, the modulation potential $\phi(t)$ in units of an electric potential (eV). Thus, the differential flux of primaries at Earth only depends on the particle type, the solar activity, and the LIS, which has been parameterized based on numerical simulations and fitting observations for protons and for electrons. In the following, we use the LIS proposed by *[Herbst et al., 2017]* for protons and alphas, taking Voyager I data into account as follows:

$$J_{LIS}(E) = \begin{cases} 0.707\exp\left(4.64 - 0.036(\ln E)^2 - 2.91\sqrt{E}\right) \; if \; E < 1.4\; GeV, \\ 0.685\exp(3.22 - 2.78(\ln E) - 1.5/E) \; if \; \geq 1.4\; GeV, \end{cases} \quad (33)$$

In addition, to take into account the effect of the Earth's geomagnetic field, we compare the rigidity of the primary particles ($R = pc/q$ with p the momentum of the particle, q the electric charge of the particle and c is the speed of light) and the effective vertical rigidity cutoff (R_c) at a given location on the Earth. If for a given particle $R < R_c$, then the particle will not be able to reach the TOA. Thus, the flux of primary particles that contribute to ionization and dose is effectively given by: $\frac{dJ}{dE}(E(R),\Phi)$ for $R \geq R_c$. The conversion between particle energy and rigidity is computed as follows:

$$R = \frac{A}{Z}\sqrt{E^2 + 2EE_0}, \quad (34)$$

where A is the mass number, Z is the charge, E_0 is the rest energy per nucleon and E is the kinetic energy of the particle per nucleon. Once the flux of primary particles at the top of the atmosphere is computed and matches the energy dimension of the ARM, the resulting ionization or/and dose rate profiles can be computed by multiplying the ARM with the TOA flux for each species:

$$\boldsymbol{P}(h) = \sum_i \boldsymbol{M_i}(E,h) \cdot \boldsymbol{F}_i(E), \tag{35}$$

where P is the ionization or dose profile (which has the dimension of altitudes) and $F_i(E) = j_i(\mathrm{E})\Omega A$ is the number of primary particles in [#/s] at TOA. In this case, j is the differential flux of the primary particles in [$cm^{-2}sr^{-1}MeV^{-1}$], Ω is the integration of the cosine of the zenith angle of the primary particles ($\Omega = \pi$) and A [cm^2] is the surface area of the top of the atmosphere. In this case, i denotes the type of primary particles. The same can be done to compute atmospheric dose rates, as illustrated in Fig. 20.

4.3.2 Secondary particles

When AtRIS is running in the default mode *(-1)*, the results of the simulations are the atmospheric response matrices discussed above. However, it is also possible to run AtRIS in 'secondary mode' *(0)*. In this case, an additional file is created by the simulation. It contains information on all the particles passing from one atmospheric volume to another. For each particle, all information about its type, altitude, propagation direction, kinetic energy, and primary vertex energy is written over 16 bytes (see Table 2 for more details).

Data	Data type	Data size (byte)
Particle Data Group Code	Int	4
Interface id (iid)	unsigned int	2
Direction	unsigned int	2
secondary particle energy [MeV]	float	4
primary vertex energy [MeV]	float	4

Table 2: Information contained in the binary file created by AtRIS when it runs in mode=0.

It is important to note that running AtRIS in this mode means that the size of the simulation output is considerably larger than in the default mode. For instance, running AtRIS in mode *'0'* with primary protons with energy ranging from 1 MeV to 1 TeV in 120 bins, injecting 2500 particles per bin in an atmosphere ranging from 0 km to 100 km in 200 layers results in a ~ 100 GB file. Knowing that the file of each secondary particles has the size of 16 bytes, it follows that the number of simulated particles is ~ 6.25 billion. If the same simulation is run with primary alpha particles, then the size of the file reaches ~ 400 GB. From this file, it is possible to compute the spectrum of the secondaries at a given altitude. This process is explained in detail *in [Guo et al., 2019].* For a given particle type (fixed PDGC), altitude, and propagation direction, it is possible to create a response matrix (2D-histogram) that relates the primary particle energy and the secondary particle energy. The idea is to build a response matrix H^{sp} that statistically describes the transformation of a spectrum of primary particles $j^p(E^0)$ of type p at the top of the atmosphere to a spectrum of secondary particles $j^s(E)$ of types at a given altitude, so that

$$\boldsymbol{j}^s(E) = \sum_p \boldsymbol{H}^{sp}(E,E^0) \cdot \boldsymbol{j}^p(E^0), \tag{36}$$

where both $j^s(E)$ and $j^p(E^0)$ are differential spectra expressed in [$cm^{-2}s^{-1}sr^{-1}MeV^{-1}$]. Considering an AtRIS simulation in which $N_i^p(E_i^0)_{i\in\{1,..,n\}}$ primary particles of type p are simulated in n energy bins (E_i^0). For a fixed iid level and a fixed propagation direction of secondary particles of type s, we can create a matrix $M_{sp}(E,E^0)$ of size(m,n), where m is the number of energy bins (E_j). Each element H_{ij}^{ps} of the matrix gives the number of secondary particles

of type s in the energy bin E_j that were created by N_i^p primary particles of type p in the energy bin E_i^0. The final matrix H^{sp} in Fig. 23 is built from the matrix M_{sp} in the following way:

$$\boldsymbol{H}_{ji}^{sp}\left(E_j, E_i^0\right) = \frac{\boldsymbol{M}_{ji}^{sp}\left(E_j, E_i^0\right)}{N_i^p(E_i^0)} \frac{\Omega_{in} A_{in}}{\Omega_{out} A_{out}} \frac{W(E_i^0)}{W(E_j)} \tag{37}$$

where $N_i^p(E_i^0)$ is the number of simulated primary particles in each energy bin, Ω_{in} is the integration of the cosine of the zenith angle of the source particles, A_{in} is the area of the surface through which primary particles are fed in the simulation, $W(E_i^0)$ is the width of the primary energy bins, Ω_{out} is the integration of the cosine of the zenith angle of secondaries, A_{out} is the area of the surface that the secondary particles pass through

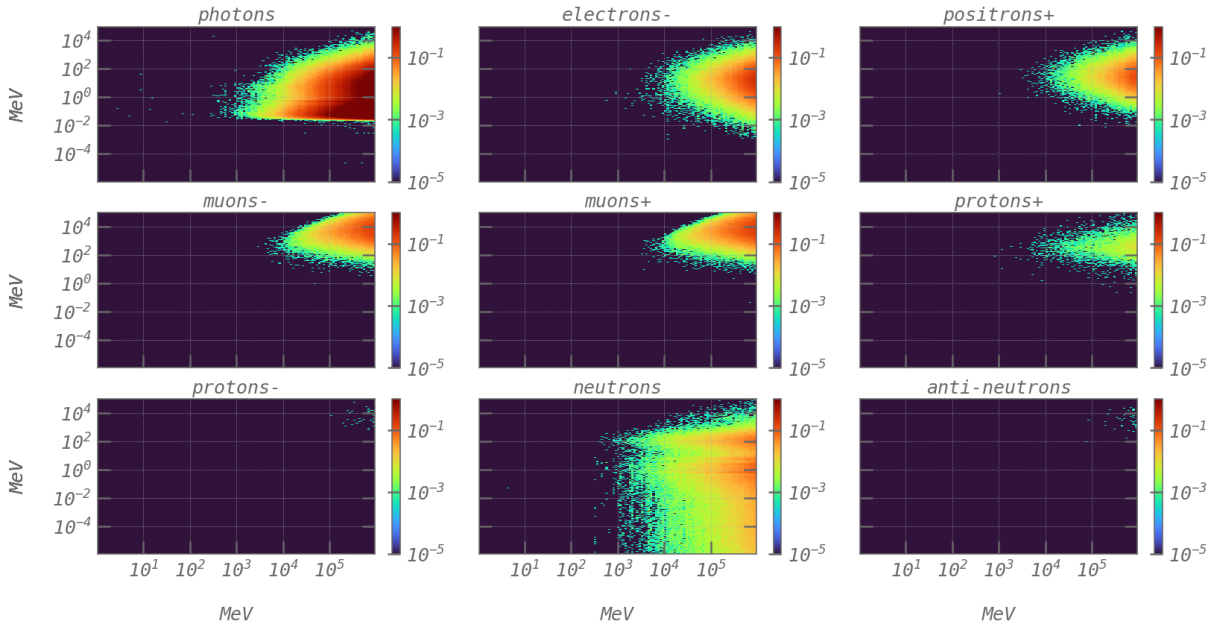

Figure 22: Example of normalized histograms for various secondary particles computed from the AtRIS binary file with iid=6 (corresponding to an altitude of 3 km). In this case, the primary particles are protons

(i.e. the area of the iid). In the case of AtRIS, in which the atmosphere is a sphere, $A_{in} = 4\pi R_{TOA}^2$ where R_{TOA}^2 is the radius of the top of the atmosphere. $\Omega_{in} = \pi$ when the primary particles are injected isotopically inward from the source sphere. For secondary particles, $A_{out} = 4\pi R_{iid}^2$ with R_{iid} is the radius of a given interface (iid). When all secondaries are propagating downward on the flux-weighted solid angle, Ω_{out}, it is the same if the secondary particles propagate upward. If the secondary particles are propagating both upwards and downwards, then $\Omega_{out} = 2$. Note that, written in this way, the matrix is dimensionless. From this matrix, it is possible to compute the integral flux of a given particle type or its energy spectrum. From the retrieved differential flux of secondary particles, it is possible to compute the integral spectrum as:

$$\boldsymbol{J}(E_j) = \boldsymbol{j}(E_j) W(E_j), \tag{38}$$

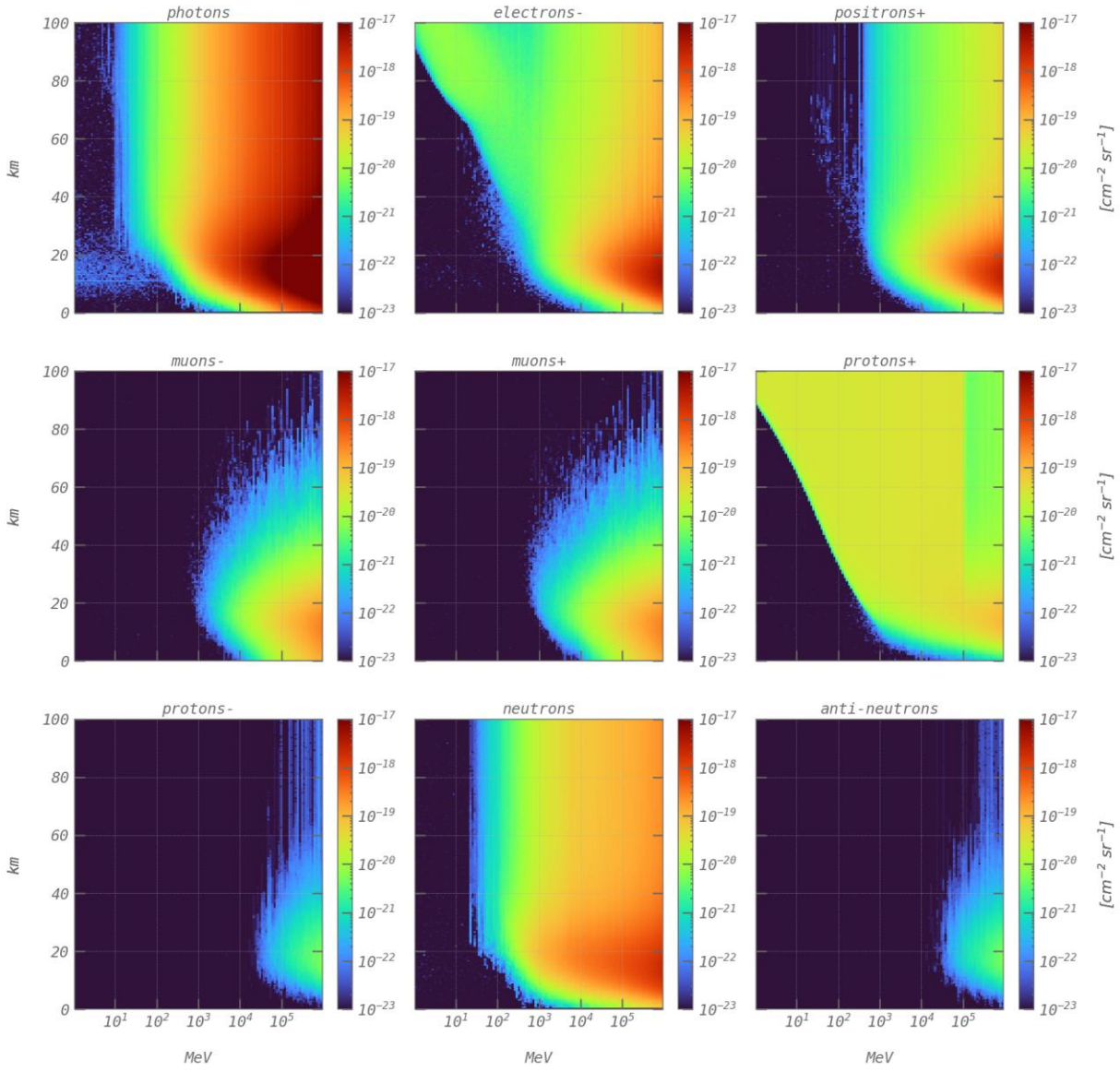

Figure 23: Example of the integral energy spectrum $\boldsymbol{R}^{sp}(E_0, h)$ of various secondary particles as a function of the altitude. As for Fig. 24, those histograms are computed from simulations with protons as primary particles.

and the lethargy spectrum as:

$$\boldsymbol{L}(E_j) = \boldsymbol{j}(E_j)\bar{E}_j, \tag{39}$$

with $W(E_i)$ the width of the secondary particle energy bins and $\bar{E}_j$ is the mean energy of the bin.

If the histograms of secondary particles are computed for each altitude level, an analogous response matrix to the ionization and dose ARMs can be built for secondary particles as follows:

$$\boldsymbol{R}_{iz}^{sp}(E_i^0, h_z) = \sum_j \frac{\boldsymbol{M}_{ji}^{sp}(E_j, E_i^0, h_z)}{N_i^p(E_i^0)\,\Omega_{out} A_{out}}, \tag{40}$$

In this case, the response matrix $R^{sp}(E^0, h)$ is expressed in [$cm^{-2}sr^{-1}$]. An example of the Secondary Atmospheric Response Matrix (SARM) is shown in Fig. 23. Then the profile of the integral secondary particle flux is given as follows:

$$\boldsymbol{P}^s(h) = \sum_p \boldsymbol{R}_{iz}^{sp}(E_i^0, h_z) \cdot \boldsymbol{F}^p(E^0), \tag{41}$$

where $F_p(E) = j_p(E)\Omega A$ is the number of primary particles in [#/*s*] at the TOA.

5 Conclusions

This Guide provides useful explanations on the way to use satellite data of particle fluxes and to define appropriate conditions for simulations of particles interacting with the atmosphere. Such clarifications are often not provided in scientific articles that assume background is known and focus more on scientific results. The guide can be useful for new users of such data and simulations. It provides also useful references where more details can be found.

6 References

[Agostinelli et al., 2003] Agostinelli, S., Allison, J., Amako, K., Apostolakis, J., Araujo, H., Arce, P., Asai, M., Axen, D., Banerjee, S., Barrand, G., et al. (2003). Geant4—a simulation toolkit. Nuclear instruments and methods in physics research section A: Accelerators, Spectrometers, Detectors and Associated Equipment, 506(3):250–303.

[Allison et al., 2006] Allison, J., Amako, K., Apostolakis, J., Araujo, H., Dubois, P. A., Asai, M., Barrand, G., Capra, R., Chauvie, S., Chytracek, R., et al. (2006). Geant4 developments and applications. IEEE Transactions on Nuclear Science, 53(1):270–278.

[Allison et al., 2016] Allison, J., Amako, K., Apostolakis, J., Arce, P., Asai, M., Aso, T., Bagli, E., Bagulya, A., Banerjee, S., Barrand, G., et al. (2016). Recent developments in Geant4. Nuclear instruments and methods in physics research section A: Accelerators, Spectrometers, Detectors and Associated Equipment, 835:186–225.

[Baker et al., 2014] Baker, D. N., Jaynes, A. N., Hoxie, V. C., Thorne, R. M., Foster, J. C., Li, X., ... & Lanzerotti, L. J. (2014). An impenetrable barrier to ultrarelativistic electrons in the Van Allen radiation belts. *Nature*, *515*(7528), 531-534.

[Banjac et al., 2019a] Banjac, S., Herbst, K., and Heber, B. (2019a). The Atmospheric Radiation Interaction Simulator (AtRIS): Description and validation. Journal of Geophysical Research: Space Physics, 124:50–67.

[Banjac et al., 2019b] Banjac, S., Herbst, K., and Heber, B. (2019b). On-the-fly calculation of absorbed and equivalent atmospheric radiation dose in a water phantom with the Atmospheric Radiation Interaction Simulator (AtRIS). Journal of Geophysical Research: Space Physics, 124:50–67.

[Botek et al., 2023] Botek, E., Pierrard, V., and Winant, A. (2023). Prediction of radiation belts electron fluxes at a low earth orbit using neural networks with PROBA-V/EPT data. Space Weather, 21(e2023SW003466).

[Cyamukungu et al., 2014] Cyamukungu, M., Benck, S., Borisov, S., Bonnet, L., Grégoire, G., Cabrera, J., Desoete, B., Semaille, C., DeSaedeleer, J., Creve, G., Van Ransbeek, E., Maes, J., Bonnewijn, S., Neefs, E., Pierrard, V., Lemaire, J., Moreau, D., Anciaux, M., Helderweirt, A., Litefti, K., Nieminen, P., Valtonen, E., Punkkinen, R., and Wojtek, H. (2014). The Energetic Particle Telescope (EPT) on board PROBA-V: description of a new science-class instrument for particle detection in space. IEEE Transactions on Nuclear Science, 61(6):3667–3681.

[Dahmen et al., 2022] Dahmen, N., Sicard, A., Brunet, A., Santolik, O., Pierrard, V., Botek, E., and Darrouzet, F. (2022). Farwest: Efficient computation of wave-particle interactions for a dynamic description of the electron radiation belt diffusion. Journal of Geophysical Research: Space Physics, 127(19):e2022JA030518.

[Gaisser et al., 2016] Gaisser, T. K., Engel, R., and Resconi, E. (2016). Cosmic Rays and Particle Physics. Cambridge University Press.

[Guo et al., 2019] Guo, J., Banjac, S., Röstel, L., Terasa, J. C., Herbst, K., Heber, B., and Wimmer-Schweingruber, R. F. (2019). Implementation and validation of the GEANT4/AtRIS code to model the radiation environment at Mars. Journal of Space Weather and Space Climate, 9:A2.

[Herbst et al., 2017] Herbst, K., Muscheler, R., and Heber, B. (2017). The new local interstellar spectra and their influence on the production rates of the cosmogenic radionuclides ^{10}Be and ^{14}C. Journal of Geophysical Research: Space Physics, 122(1):23–34.

[Ivanchenko et al., 2011] Ivanchenko, V., Apostolakis, J., Bagulya, A. V., Abdelouahed, H. B., Black, R., Bogdanov, A., Burkhard, H., Chauvie, S., Cirrone, G. A. P., Cuttone, G., et al. (2011). Recent improvements in Geant4 electromagnetic physics models and interfaces. Progress in Nuclear Science and Technology, 2:898–903.

[Klein and Dalla, 2017] Klein, K.-L. and Dalla, S. (2017). Acceleration and propagation of solar energetic particles. Space Science Reviews, 212(3):1107–1136.

[Koskinen, 2011] Koskinen, H. E. (2011). Magnetospheric storms and substorms. In Physics of Space Storms, pages 323–370. Springer.

[Koskinen and Kilpua, 2022] Koskinen, H. E. J. and Kilpua, E. K. J. (2022). Physics of Earth's Radiation Belts. Springer.

[Lopez Rosson and Pierrard, 2017] Lopez Rosson, G. and Pierrard, V. (2017). Analysis of proton and electron spectra observed by EPT/PROBA-V in the South Atlantic Anomaly. Advances in Space Research, 60(4):796–805.

[McIlwain, 1961] McIlwain, C. E. (1961). Coordinates for mapping the distribution of magnetically trapped particles. Journal of Geophysical Research, 66(11):3681–3691.

[Picone et al., 2002] Picone, J., Hedin, A., Drob, D. P., and Aikin, A. (2002). NRLMSISE00 empirical model of the atmosphere: Statistical comparisons and scientific issues. Journal of Geophysical Research: Space Physics, 107(A12):SIA–15.

[Pierrard, 2009] Pierrard, V. (2009). L'Environnement Spatial de la Terre. Presses universitaires de Louvain.

[Pierrard, 2024] Pierrard, V. (2024). Effects of the Sun on the space environment of the Earth. Presses universitaires de Louvain.

[*Pierrard et al., 2019*] Pierrard V., G. Lopez Rosson, E. Botek, Dynamics of Megaelectron Volt Electrons Observed in the Inner Belt by PROBA-V/EPT, Journal of Geophysical Research: Space Physics, 124, 1651-1659, doi: 10.1029/2018JA026289, 2019.

[Pierrard et al., 2023] Pierrard, V., Benck, S., Botek, E., Borisov, S., and Winant, A. (2023). Proton Flux Variations During Solar Energetic Particle Events, Minimum and Maximum Solar Activity, and Splitting of the Proton Belt in the South Atlantic Anomaly. Journal of Geophysical Research: Space Physics, 128, e2022JA031202.

[Pierrard et al., 2025a] Pierrard, V., Bolsée, D., Winant, A., Krasniqi, F., Al-Qaaod, A., Péters de Bonhome, M., Botek, E., Van Laeken, L., Sapundjiev, D., Van Malderen, R., Mangold, A., Ambrozova, I., Sommer, M., Slegl, J., Geronikolou, S., Georgakilas, A., Dorn, A., Rapp, B., Solc, J., Marek, L., Oancea, C., Doppler, L., Langer, R., Sabia, M., Vuolo, M., and Granja, C. (2025a). Biosphere measurement campaign from January 2024 to March 2024 and in May 2024: Effects of the solar events on the radiation belts, UV radiation and ozone in the atmosphere. AIMS Geoscience, 1(11):117–154.

[Pierrard et al., 2021a] Pierrard, V., Botek, E., and Darrouzet, F. (2021a). Improving predictions of the 3D dynamic model of the plasmasphere. Front. In Astron. Space Sci, 8:681401.

[Pierrard et al., 2020] Pierrard, V., Botek, E., Ripoll, J.-F., and Cunningham, G. (2020). Electron dropout events and flux enhancements associated with geomagnetic storms observed by PROBA-V/Energetic Particle Telescope from 2013 to 2019. Journal of Geophysical Research: Space Physics, 125(12):e2020JA028487.

[Pierrard et al., 2014] Pierrard, V., Lopez Rosson, G., Borremans, K., Lemaire, J., Maes, J., Bonnewijn, S., Van Ransbeeck, E., Neefs, E., Cyamukungu, M., Benck, S., et al. (2014). The Energetic Particle Telescope: first results. Space Science Reviews, 184(1-4):87–106.

[Pierrard et al., 2021b] Pierrard, V., Ripoll, J.-F., Cunningham, G., Botek, E., Santolik, O., Thaller, S., Kurth, W. S., and Cosmides, M. (2021b). Observations and Simulations of Dropout Events and Flux Decays in October 2013: Comparing MEO Equatorial with LEO Polar Orbit. Journal of Geophysical Research: Space Physics, 126(6):e2020JA028850.

[Pierrard et al., 2025b] Pierrard, V., Verhulst, T., Chevalier, J.-M., and Bergeot, N.and Winant, A. (2025b). Effects of the Geomagnetic Superstorms of 10–11 May 2024 and 7–11 October 2024 on the Ionosphere and Plasmasphere. Atmosphere, 16(299).

[Pierrard et al., 2024] Pierrard, V., Winant, A., Botek, E., and Péters de Bonhome, M. (2024). The Mother's Day Solar Storm of 11 May 2024 and its Effect on Earth's Radiation Belts. Universe, 391(10):10.

[Ukhorskiy and Sitnov, 2012] Ukhorskiy, A. and Sitnov, M. (2012). Dynamics of Radiation Belt Particles. The Van Allen Probes mission, pages 545–578.

[Winant et al., 2023] Winant, A., Pierrard, V., Botek, E., and Herbst, K. (2023). The Atmospheric Influence on Cosmic-Ray-Induced Ionization and Absorbed Dose Rates. Universe, 9(12):502.

[Winant et al., 2025] Winant A., Pierrard V., Botek E., Ozone decrease observed in the upper atmosphere following the May 11th 2024 Mother's day solar storm, Annales Geophysicae, 2025, https://doi.org/10.5194/angeo-2024-29